Cell Metabolism

Article

Targeting gut microbial nitrogen recycling and cellular uptake of ammonium to improve bortezomib resistance in multiple myeloma

Graphical abstract

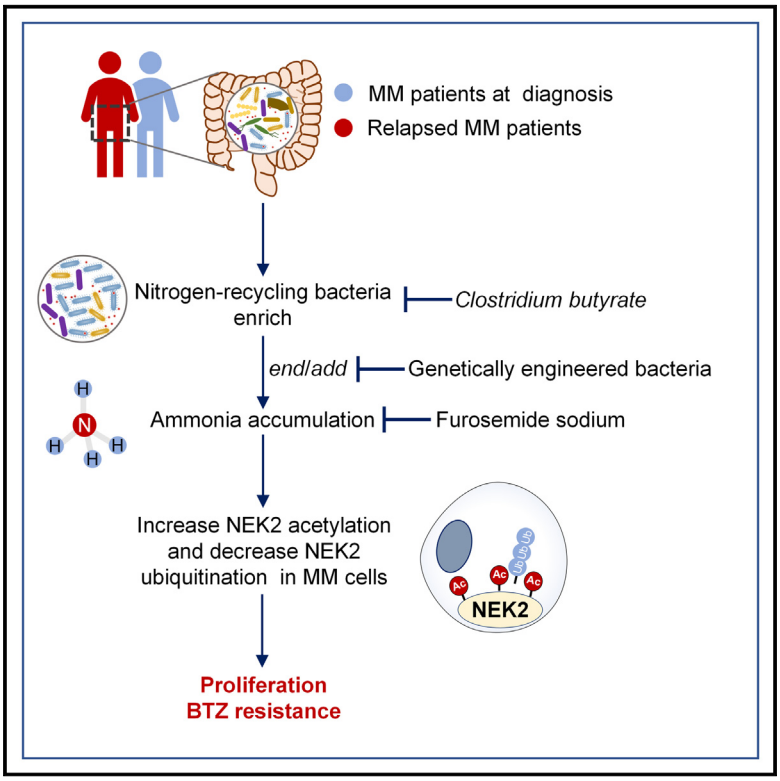

Authors

Yinghong Zhu, Xingxing Jian, Shuping Chen, ..., Wei Jia, Yanjuan He, Wen Zhou

Correspondence

chenxiangck@126.com (X.C.), weijia1@hkbu.edu.hk (W.J.), yjuanh@csu.edu.cn (Y.H.), wenzhou@csu.edu.cn (W.Z.)

In brief

Zhu et al. demonstrated that *Citrobacter freundii* induces bortezomib resistance in patients with multiple myeloma by elevating circulating ammonium level. The increased ammonium enters myeloma cells, enhancing the stability of NEK2 protein. Notably, the administration of furosemide and probiotics such as *Clostridium butyricum* was observed to partially alleviate bortezomib resistance.

Highlights

- *Citrobacter freundii* can induce bortezomib resistance in patients with multiple myeloma
- Ammonium can enhance NEK2 stability, inducing bortezomib resistance of myeloma cells
- Furosemide administration can attenuate bortezomib resistance of myeloma cells
- Probiotics like *Clostridium butyricum* alleviate myeloma cell resistance to bortezomib

Zhu et al., 2024, Cell Metabolism *36*, 159–175
January 2, 2024
https://doi.org/10.1016/j.cmet.2023.11.019

CellPress

Cell Metabolism

CellPress
OPEN ACCESS

Article

Targeting gut microbial nitrogen recycling and cellular uptake of ammonium to improve bortezomib resistance in multiple myeloma

Yinghong Zhu,[1,2,9] Xingxing Jian,[1,7,9] Shuping Chen,[1] Gang An,[3] Duanfeng Jiang,[4] Qin Yang,[4] Jingyu Zhang,[1,2] Jian Hu,[1] Yi Qiu,[1] Xiangling Feng,[5] Jiaojiao Guo,[1,2] Xun Chen,[1,2] Zhengjiang Li,[1,2] Ruiqi Zhou,[1,2] Cong Hu,[1,2] Nihan He,[1,2] Fangming Shi,[1,2] Siqing Huang,[1,2] Hong Liu,[7] Xin Li,[4] Lu Xie,[1] Yan Zhu,[1] Lia Zhao,[1] Yichuan Jiang,[1] Jian Li,[6] Jinuo Wang,[6] Lugui Qiu,[3] Xiang Chen,[7,*] Wei Jia,[8,*] Yanjuan He,[1,*] and Wen Zhou[1,2,5,10,*]

[1]Haihe Laboratory of Cell Ecosystem, State Key Laboratory of Experimental Hematology, Bioinformatics Center, National Clinical Research Center for Geriatric Disorders, Key Laboratory for Carcinogenesis and Invasion, Chinese Ministry of Education, Key Laboratory of Carcinogenesis, Chinese Ministry of Health, Furong Laboratory, Department of Hematology, Xiangya Hospital, Central South University, Changsha, Hunan, China

[2]Cancer Research Institute, School of Basic Medical Sciences, Central South University, Changsha, Hunan, China

[3]State Key Laboratory of Experimental Hematology, Institute of Hematology & Blood Diseases Hospital, Chinese Academy of Medical Science & Peking Union Medical College, Tianjin, China

[4]Department of Hematology, Third Xiangya Hospital, Central South University, Changsha, Hunan, China

[5]Xiangya School of Public Health, Central South University, Changsha, Hunan, China

[6]Peking Union Medical College Hospital, Chinese Academy Medical Society & Peking Union Medical College, Beijing, China

[7]Department of Dermatology, Xiangya Hospital, Central South University, Changsha, Hunan, China

[8]School of Chinese Medicine, Hong Kong Baptist University, Kowloon Tong, Hong Kong, China

[9]These authors contributed equally

[10]Lead contact

*Correspondence: chenxiangck@126.com (X.C.), weijia1@hkbu.edu.hk (W.J.), yjuanh@csu.edu.cn (Y.H.), wenzhou@csu.edu.cn (W.Z.)

https://doi.org/10.1016/j.cmet.2023.11.019

SUMMARY

The gut microbiome has been found to play a crucial role in the treatment of multiple myeloma (MM), which is still considered incurable due to drug resistance. In previous studies, we demonstrated that intestinal nitrogen-recycling bacteria are enriched in patients with MM. However, their role in MM relapse remains unclear. This study highlights the specific enrichment of *Citrobacter freundii* (*C. freundii*) in patients with relapsed MM. Through fecal microbial transplantation experiments, we demonstrate that *C. freundii* plays a critical role in inducing drug resistance in MM by increasing levels of circulating ammonium. The ammonium enters MM cells through the transmembrane channel protein SLC12A2, promoting chromosomal instability and drug resistance by stabilizing the NEK2 protein. We show that furosemide sodium, a loop diuretic, downregulates SLC12A2, thereby inhibiting ammonium uptake by MM cells and improving progression-free survival and curative effect scores. These findings provide new therapeutic targets and strategies for the intervention of MM progression and drug resistance.

INTRODUCTION

Multiple myeloma (MM) is characterized by the proliferation of malignant plasma cells secreting excessive monoclonal immunoglobulin.[1–4] Despite advancements in treatments with proteasome inhibitors (PIs), immunomodulatory drugs, and monoclonal antibodies, MM remains incurable due to drug resistance and relapse.[1] Earlier efforts to decipher the genetic/epigenetic basis of MM revealed the crucial role of bone marrow microenvironment (BMME) components in cell survival and drug resistance.[5,6] Our research linked NEK2 to poor survival and drug resistance in MM by activating multidrug resistance proteins, autophagy, and self-renewal.[7–9] Elevated glycine in the BMME also promotes MM progression.[10] However, additional perspectives are required to fully grasp the molecular mechanisms driving MM initiation, development, and maintenance.

In the last decade, researchers have linked gut microbiota to carcinogenesis and chemo- or immunotherapy response.[11] Gut microorganisms influence the cancer cell response to chemotherapeutics by affecting nucleotide synthesis and the autophagy pathway.[12,13] Bacteria and their products also impact immunotherapies by targeting myeloid cells or T cells.[14,15] These findings illustrate potential crosstalk between cancer cells and gut microorganisms during therapies. Specific gut species like *Prevotella heparinolytica* and *Eubacterium hallii* are reported to be related to MM progression.[16,17] We also demonstrated that intestinal nitrogen-recycling bacteria, such as *Klebsiella pneumoniae*, were enriched in newly diagnosed MM patients,

accelerating disease development and pneumonia incidence through synthesizing L-glutamine.[18,19]

Despite the proven efficacy of the PI bortezomib (PS-341, BTZ) against MM,[20–23] several mechanisms of resistance have been reported, including PSMB5 mutations,[24] autophagy,[25,26] ubiquitin proteasome system,[27] antioxidant response,[10,28] and metabolic pathways.[29–32] However, the potential influence of the gut microbiota on resistance against first-line drugs such as BTZ in MM patients remains unclear. Our current study delves into the molecular mechanisms of MM drug resistance using cell lines, mouse models, and clinical samples. We identify new modulators and signaling pathways influencing MM progression, offering insights into therapeutic targets and intervention strategies for MM.

RESULTS

Gut bacterial species exhibit differential abundance between patients with MM and healthy controls

We previously showed that nitrogen-recycling bacteria are significantly enriched in patients with MM at diagnosis (ADs) and accelerate proliferation of MM cells.[18] To further explore the role of the gut microbiome in relapsed patients with MM (RMs), we collected additional age- and gender-matched feces from 20 healthy controls (HC), 28 ADs, and 17 RMs for metagenomic sequencing and bioinformatics analysis.

We performed principal coordinate analysis (PCoA) to present the β-diversities and found that the composition of gut bacterial species differed significantly among the three groups (Figure 1A). Additionally, the α-diversity at the bacterial species level was significantly lower in HCs compared with ADs and RMs, while no significant difference was found between ADs and RMs (Figure 1B).

To identify the key specific gut microbes with differential abundances, we screened the core microbes in the three groups separately and then united all core microbes. At the genus level, most core genera were shared among the three groups (Figure S1A), and those core genera with differential abundance were identified in MM patients versus HCs and in RMs versus ADs (Figure S1B; Table S1). Comparison of the samples of HCs, ADs, and RMs revealed the gradual increase of abundance of 6 core genera (Figure S1C). Similarly, most core species were also shared (Figure S1D), and those core species with differential abundance were also identified in MM patients versus HCs and in RMs versus ADs (Figure S1E; Table S1), and 13 species showed a gradual enrichment in RMs (Figure 1C).

Citrobacter freundii correlates with MM relapse and induces bortezomib resistance

To identify the gut bacterial species that are highly enriched in RMs, we treated the 13 species enriched in RMs individually as features for receiver operating characteristic (ROC) analysis and identified 3 species—*Citrobacter freundii* (*C. freundii*), *Klebsiella oxytoca* (*K. oxytoca*), and *Raoultella ornithinolytica* (*R. ornithinolytica*)—with a greater area under the curve (AUC) in MM patients versus HCs and in RMs versus ADs (Figure 1D). In an independent cohort, higher relative abundance of the three species (in RMs than in ADs) was validated (Figure 1E). Moreover, while paired RM samples also showed higher *C. freundii* and *R. ornithinolytica* than AD samples (Figures 1F, S1F, and S1H), only *C. freundii* correlated negatively with the time to relapse in ADs (Figures 1G, S1G, and S1I). We then divided RM samples into two groups based on the median abundance of each of these three species and found that the patients with high *C. freundii* had a significantly higher average number of treatment lines (Figures 1H and S1J). In particular, RMs with higher *C. freundii* received more treatment lines (Figure 1I) and exhibited a higher average Durie-Salmon (DS) myeloma stage (Table S2). These findings indicate that the abundance of *C. freundii* is linked to the likelihood of MM relapse. Moreover, significantly reduced *C. freundii* was observed after remission compared to those patients with MM (ADs and RMs) before chemotherapy, suggesting a potential association between *C. freundii* and patient remission (Figure S1K).

Does the alteration of gut microbes in patients with MM play a functional role in drug resistance? To address this question, we performed a fecal microbiota transplantation (FMT) experiment in which fecal microbiota from AD1 or RM1 were transplanted by gavage into mice with luciferase-expressing MM tumors (Figure 2A). We detected higher luminescence intensity (Figures 2B and 2C) and serum IgG2b content (Figure 2D) in the AD1 group than in the vehicle (PBS)-treated control group, suggesting that gut microbiota from AD1 accelerated the development of MM in the AD1-FMT mice. As expected, BTZ treatment effectively inhibited the development of MM (Figures 2B–2D). Interestingly, luminescence intensity and serum IgG2b were significantly increased in BTZ-treated RM1-FMT mice (RM1+BTZ) compared to BTZ-treated control (BTZ) and AD1-FMT (AD1+BTZ) mice (Figures 2B–2D), suggesting that the gut microbiota from RMs attenuated the anti-tumor effects of BTZ. We then collected those mice feces to measure *C. freundii*, *K. oxytoca*, and *R. ornithinolytica*. Interestingly, although *C. freundii* was correlated positively with *K. oxytoca* and *R. ornithinolytica*, only the change in *C. freundii* correlated consistently with the alteration in tumor burden (as revealed by luminescence intensity and serum IgG2b) in MM mice (Figures 2E and S2A–S2C). Similar results were also obtained from two additional FMT experiments (Figures S2D–S2L).

Next, we performed single bacterium colonization (SBC) experiments in mice with luciferase-expressing MM tumors to determine whether *C. freundii* plays a causal role in the development of BTZ resistance in MM cells (Figure 2F). *C. freundii* successfully colonized the mice denoted as the CFr and the CFr+BTZ groups (Figure 2G). We subsequently examined tumor luminescence (Figures 2H and 2I) and serum IgG2b (Figure 2J) and found that the CFr+BTZ mice exhibited heavier tumor burden compared to the BTZ mice (Figures 2H–2J), indicating that the increase of *C. freundii* could cause MM cells to become resistant to BTZ. We also collected feces from the transplanted mice to confirm that *C. freundii* did accumulate as a result of transplantation (Figure 2K). Additional SBC experiments were conducted to confirm the effect of *C. freundii* on MM drug resistance (Figures S2M and S2N).

In addition, we performed SBC experiments for *K. oxytoca* and *R. ornithinolytica* to explore their contribution to MM relapse (Figure S2O). The higher tumor burden quantified by tumor luminescence and serum IgG2b was shown in the ROr+BTZ mice compared to the BTZ mice (Figures S2P–S2R), while the KOx+BTZ mice exhibited little difference from the BTZ mice. Also, to

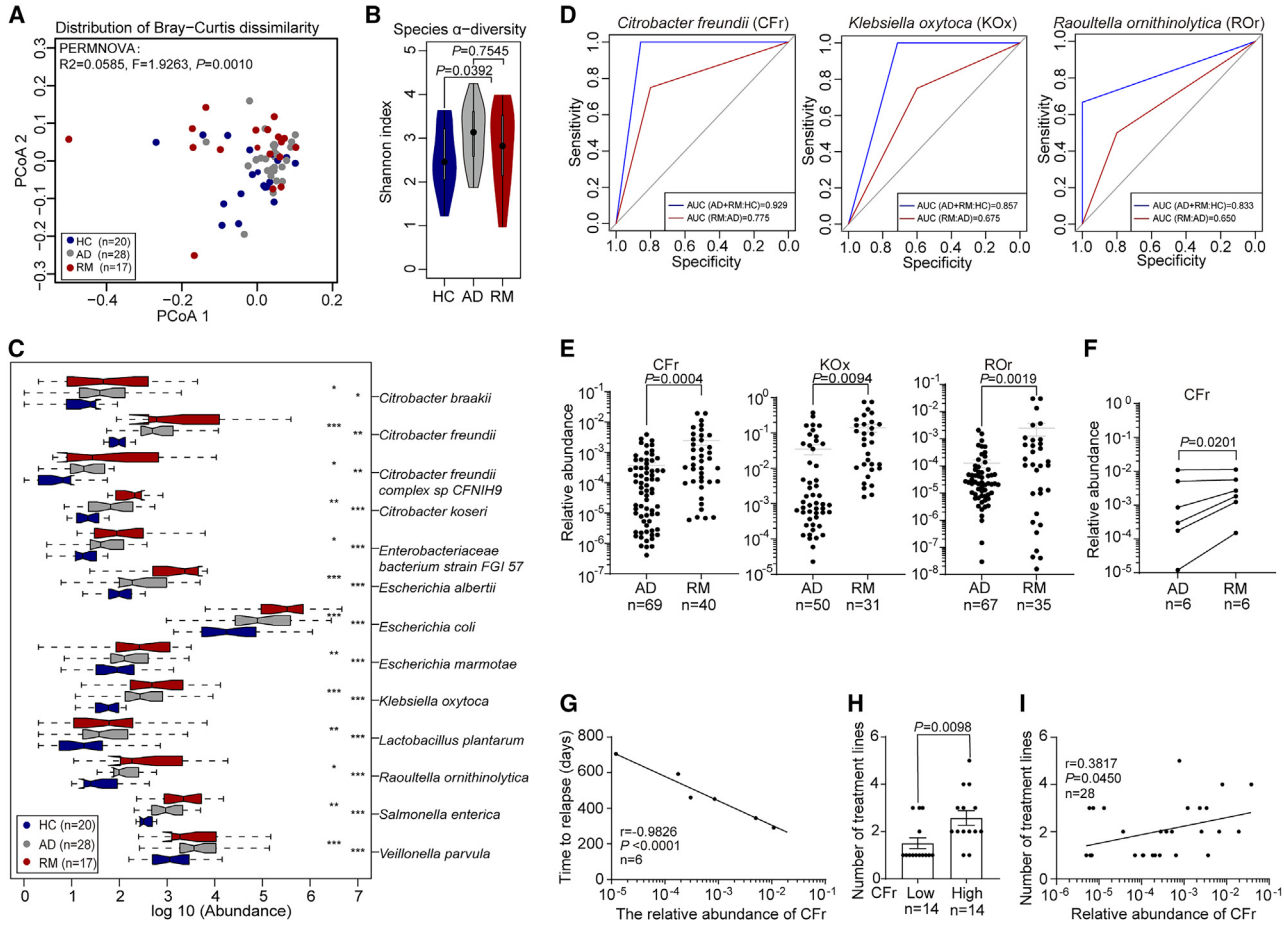

Figure 1. Higher abundance of nitrogen-recycling *Citrobacter freundii* is associated with MM relapse

(A) PCoA based on the Bray-Curtis dissimilarity index presents β-diversity among HCs, ADs, and RMs. Significance was determined by PERMANOVA (R2 = 0.0585, F = 1.9263, p = 0.001).

(B) Violin graphs show the Shannon-Wiener index of HCs, ADs, and RMs at the species level (HC, n = 20; AD, n = 28; RM, n = 17).

(C) Boxplot shows the scaled logarithm base 10 of the abundance of 13 species enriched in RMs. These differential species were identified by DESeq2 (| log2FC| > 1 and adj. p < 0.05).

(D) ROC curves depict the relative abundance of *C. freundii* (left), *K. oxytoca* (middle), and *R. ornithinolytica* (right) in HCs, ADs, and RMs (HC, n = 20; AD, n = 28; RM, n = 17).

(E) Graphs indicate species with significant differential abundance in an independent cohort verified by qPCR. Wide and short horizontal lines represent mean ± SEM; statistics used unpaired two-tailed t test.

(F) Assessment of the relative abundance of *C. freundii* in paired ADs and RMs (paired two-tailed t test).

(G) Pearson correlation of the relative abundance of *C. freundii* and the time to relapse in ADs.

(H) Graph indicates the correlation between relative abundance of *C. freundii* and the number of treatment lines in RMs. Bars represent mean ± SEM; statistics performed using unpaired two-tailed t test.

(I) Pearson correlation of the relative abundance of *C. freundii* and the number of treatment lines in RMs.

confirm the colonization of *K. oxytoca* and *R. ornithinolytica*, we detected *K. oxytoca* and *R. ornithinolytica* in feces of the transplanted mice (Figure S2S). These results indicate that like *C. freundii*, *R. ornithinolytica* can induce MM resistance to BTZ, whereas *K. oxytoca* cannot.

Citrobacter freundii induces the accumulation of NH_4^+ in MM

Since *C. freundii* are known to act as nitrogen-recycling bacteria,[18] we hypothesized that the role of *C. freundii* in nitrogen metabolism may be related to its effects on drug resistance in MM. We determined the concentrations of NH_4^+ in the cecal contents and serum of mice in SBC experiments of *C. freundii* (Figure 2F) and found that both were elevated in the CFr and CFr+BTZ mice compared with the BTZ mice (Figures 2L and 2M). Specifically, we observed strong positive correlations between cecal and serum NH_4^+ concentrations (Figure 2N) and between these concentrations and the abundance of *C. freundii* (Figure 2O). Similarly, in SBC experiments of *K. oxytoca* and *R. ornithinolytica* (Figure S2O), compared with the BTZ mice, we detected higher cecal and serum NH_4^+ levels in the ROr+BTZ mice and higher cecal NH_4^+ and unchanged serum NH_4^+ levels in

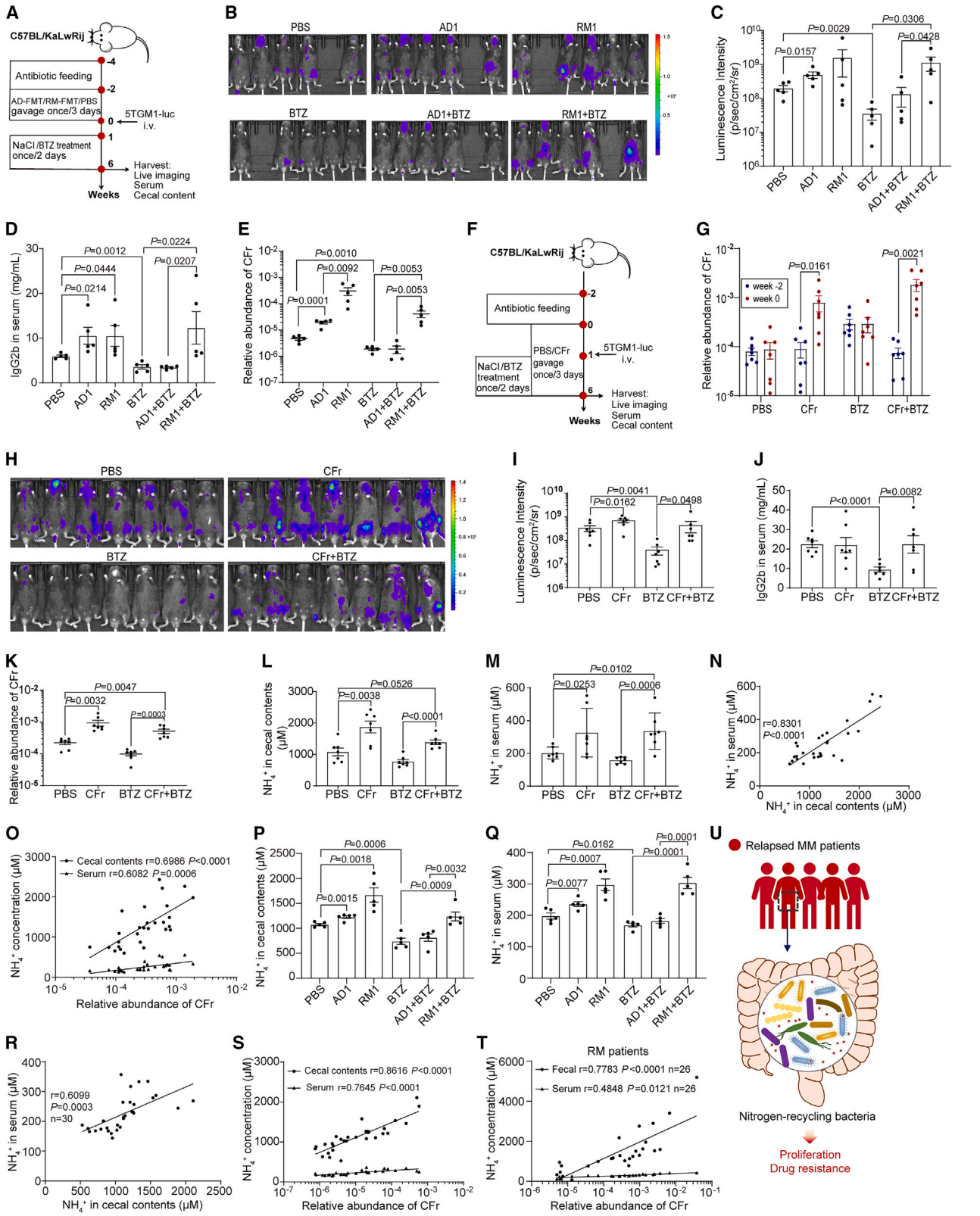

Figure 2. *Citrobacter freundii* induces resistance to bortezomib

(A) Schematics of the fecal microbiota transplantation (FMT) experiments conducted in mice injected with luciferase-expressing 5TGM1 cells to induce MM (5TGM1 MM mice).

(legend continued on next page)

the KOx+BTZ mice (Figures S2T and S2U). Also, a strong positive correlation was found between cecal and serum NH_4^+ concentrations (Figure S2V). Strong positive correlations were observed between the abundance of *R. ornithinolytica* and cecal and serum NH_4^+ concentrations, while *K. oxytoca* lacked such correlations (Figures S2W and S2X).

We next examined NH_4^+ concentrations in mice transplanted with fecal microbiota from patients with MM (Figures 2P and 2Q) and found a strong positive correlation between the NH_4^+ in cecal contents and serum (Figure 2R). We also observed the positive correlations between the abundance of *C. freundii* and the NH_4^+ in the cecal contents and serum (Figure 2S). However, we did not observe significant correlations between the abundance of *K. oxytoca* or *R. ornithinolytica* and serum NH_4^+, although we observed significant correlations between *K. oxytoca* or *R. ornithinolytica* and cecal NH_4^+ (Figures S2Y and S2Z). To extend the findings from the mouse model, we assessed the samples from RMs and discovered similar correlations between the abundance of *C. freundii* and the fecal and serum NH_4^+ concentrations (Figure 2T). Together, these results suggest that *C. freundii* mediates the accumulation of NH_4^+ in patients with MM (Figure 2U).

NH_4^+ accelerates MM progression and induces relapse

A study of 21 patients with MM showed that 38% of them had high PB NH_4^+ levels (standard limits, 10–50 μM) while 14% had neurological symptoms of encephalopathy without signs of liver dysfunction.[33] The accumulation of NH_4^+ in patients with MM led us to ask whether it plays a functional role in MM progression and/or relapse. We first determined whether there were differences in fecal and serum NH_4^+ concentrations between ADs and RMs. As expected, the RMs exhibited significantly higher fecal and serum NH_4^+ than the ADs (both paired and unpaired) (Figures 3A and 3B). Next, we divided the RM samples into two groups (low-NH_4^+ and high-NH_4^+) based on the median concentration of fecal NH_4^+ and assessed the correlations between NH_4^+ and those clinical characteristics of MM, finding that the high-NH_4^+ RMs exhibited a more advanced DS stage, indicating a comparatively elevated disease burden (Table 1). Meanwhile, we observed poorer overall and progression-free survival in the high-NH_4^+ ADs (Figures 3C and 3D; Table S3). The association between higher NH_4^+ and more advanced MM suggests that NH_4^+ accumulation may accelerate MM progression and induce relapse in ADs.

We next sought to establish a causal role for NH_4^+ in MM development and relapse. We cultured MM cell lines, including ARP1 and H929, in medium containing increasing concentrations of NH_4^+, finding that NH_4^+ maximally enhances MM cell proliferation at 0.5 mM (Figures S3A and S3B). We then supplemented this medium with BTZ and observed that addition of 0.5 mM NH_4^+ robustly reduced the anti-tumor effect of BTZ on MM cells (Figures 3E and S3B). Moreover, under the same conditions, we found that BTZ-mediated induction of MM cell apoptosis was inhibited by NH_4^+ in ARP1 and H929 cells (Figures 3F and S3C–S3E). This inhibition was also observed with adriamycin (ADM) (Figure S3F) and lenalomide (Len) (Figure S3G). These results show that NH_4^+ can enhance MM cell proliferation and attenuate the sensitivity of MM cells to BTZ/ADM/Len.

We subsequently investigated the effect of NH_4^+ on MM cell resistance to BTZ *in vivo*, using an MM mouse model induced by inoculation with ARP1 cells (Figure S3H). As expected, intragastric supplementation with NH_4Cl significantly increased tumor luminescence in BTZ-treated and -untreated ARP1 MM mice compared to un-supplemented controls (Figures S3I and S3J). Measurement of NH_4^+ in the cecal contents and serum confirmed higher NH_4^+ in the NH_4Cl-supplemented mice, verifying the effectiveness of NH_4^+ administration (Figures S3K–S3M). Notably, the concentrations of NH_4^+ in our experiments were similar to those used in earlier studies.[18]

Finally, to confirm these *in vivo* effects, we used another established MM mouse model induced by the inoculation of 5TGM1 MM cells (Figure 3G). As in the ARP1 MM mouse model, the tumor burden (as measured by tumor luminescence and serum IgG2b) was elevated when NH_4^+ was supplemented to the control or the BTZ-treated mice (Figures 3H, 3I, and S3N). In addition, NH_4^+ were significantly higher in the cecal contents and serum of NH_4Cl+BTZ mice than those in the BTZ mice, while a

(B) Live imaging of the tumor-associated luminescence intensity in 5TGM1 MM control mice (PBS), mice with FMT from AD1 (AD1), mice with FMT from RM1 (RM1), and all three groups treated with BTZ (0.75 mg/kg every 2 days).
(C) Quantification of tumor-associated luminescence intensity in the 5TGM1 MM mice cohorts shown in (B).
(D) Serum concentrations of IgG2b, determined via ELISA, in these six mouse groups (n = 5 in each group).
(E) Relative abundance of *C. freundii* in fecal samples from 5TGM1 MM mice.
(F) Schematics of the *C. freundii* transplantation experiments in 5TGM1 MM mice.
(G) Relative abundance of *C. freundii* in fecal samples from 5TGM1 MM mice before tumor inoculation.
(H) Live imaging of the tumor-associated luminescence intensity in 5TGM1 MM control mice (PBS), mice treated with *C. freundii* transplantation (CFr), and both groups treated with BTZ at week 6.
(I) Quantification of tumor-associated luminescence intensity in the 5TGM1 MM mice cohorts shown in (H).
(J) Serum concentrations of IgG2b, determined via ELISA, in these four mouse groups (n = 7 in each group) in week 7.
(K) Relative abundance of *C. freundii* in fecal samples derived from 5TGM1 MM mice in week 7.
(L and M) NH_4^+ concentrations in cecal contents (L) and serum (M) from 5TGM1 MM mice in *C. freundii* transplantation experiments.
(N and O) Pearson correlations between NH_4^+ concentrations in cecal contents and serum (N) and between relative abundance of *C. freundii* and NH_4^+ concentrations in cecal contents and serum (O) in *C. freundii* transplantation experiments (n = 28).
(P and Q) NH_4^+ concentrations in cecal contents (P) and serum (Q) from 5TGM1 MM mice in FMT experiments.
(R and S) Pearson correlation between NH_4^+ concentrations in cecal contents and serum (R) and between relative abundance of *C. freundii* and NH_4^+ concentrations in cecal contents and serum (S) in FMT experiments (n = 30).
(T) Pearson correlation between relative abundance of *C. freundii* and NH_4^+ concentrations in fecal samples and serum in RMs (n = 26).
(U) Schematics of nitrogen-recycling bacteria inducing drug resistance to BTZ in MM.
Data represent mean ± SEM in (C)–(E), (G), (I)–(M), (P), and (Q). Statistics used unpaired two-tailed t test (C–E, G, I–M, P, and Q).

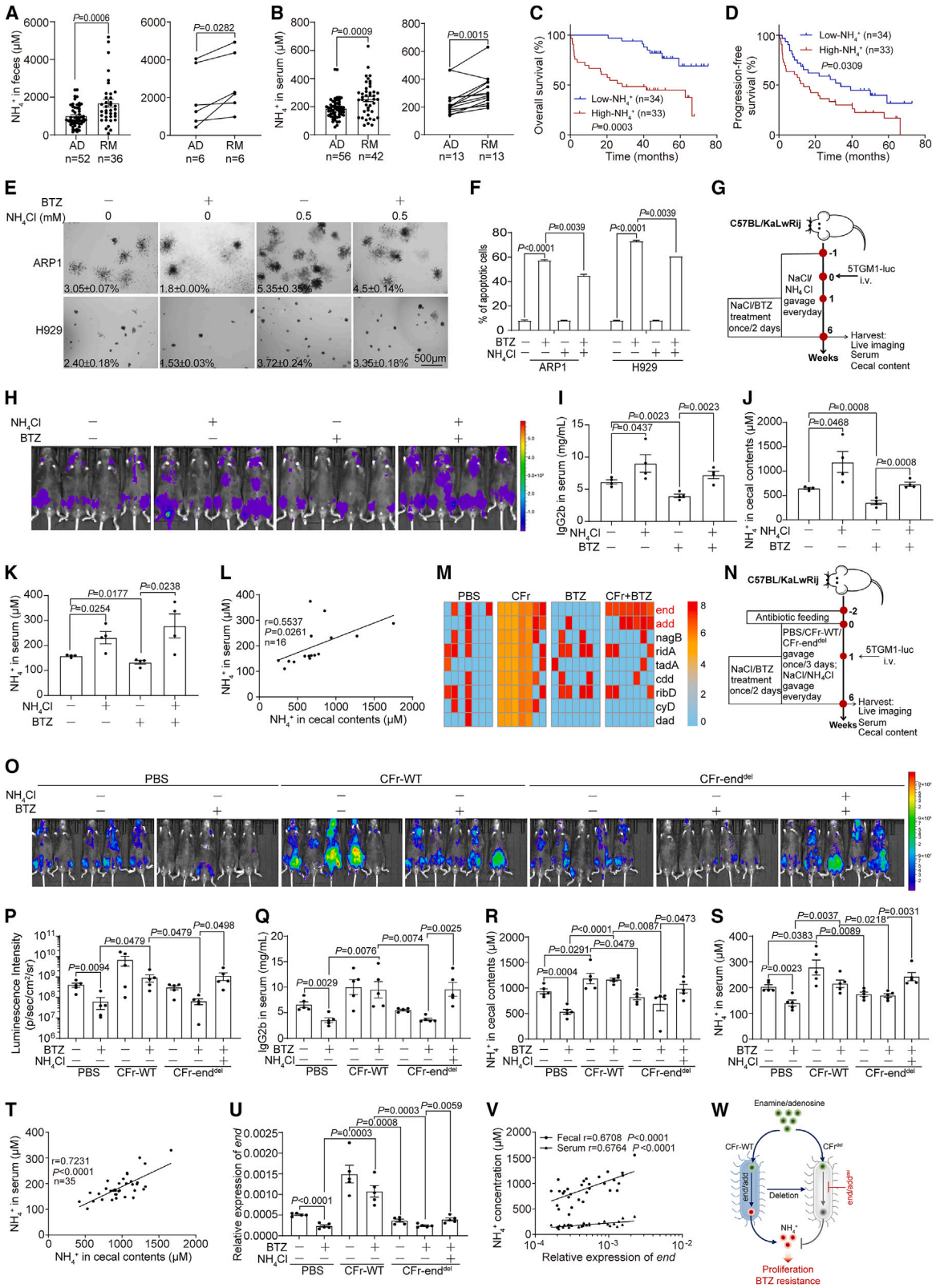

Figure 3. *Citrobacter freundii*-mediated ammonium synthesis induces resistance to bortezomib

(A) Left: NH_4^+ concentrations in fecal samples from patients with MM. Right: NH_4^+ concentrations in fecal samples derived from paired patients with MM.

(B) Left: NH_4^+ concentrations in serum derived from patients with MM. Right: NH_4^+ concentrations in serum derived from paired patients with MM.

(legend continued on next page)

strong positive correlation between the NH_4^+ in cecal contents and serum was also seen (Figures 3J–3L). Taken together, these findings indicate that NH_4^+ accelerates MM progression and induces relapse.

Citrobacter freundii increases NH_4^+ production by expressing deaminases

Having shown that *C. freundii* induces the accumulation of NH_4^+ and that NH_4^+ promotes MM progression *in vitro* and *in vivo*, we next sought to dissect the molecular mechanisms underlying *C. freundii* production of NH_4^+ during MM. First, we found that *C. freundii* produced a large amount of NH_4^+ *in vitro*, supporting our earlier findings (Figure S3O, left). Similarly, the production of NH_4^+ was observed in the fermentation liquid of *R. ornithinolytica* and *K. oxytoca* (Figure S3O, right). We next examined the *C. freundii* reference genome in the NCBI database, finding nine deaminase-encoding genes that are transcribed by *C. freundii* (Figures S3P and S3Q). Experiments that measured the relative levels of these nine genes in cecal contents from mice gavaged with *C. freundii* (Figure 2F) revealed that only two genes—*end* and *add*—were specifically and robustly expressed (Figure 3M). We therefore constructed and selected two strains with *end* or *add* deletion (i.e., CFr-add^{del} and CFr-end^{del}, respectively) (Figures S3R–S3V). We used these two strains individually for SBC experiments by gavage (Figure S4A) and subsequently detected significantly lower NH_4^+ in the cecal contents and serum of the experimental mice. The two disrupted *C. freundii* also produced much less NH_4^+ *in vivo* compared to the wild-type (WT) bacteria (Figures S4B and S4C), and this reduction was especially pronounced in CFr-end^{del}. Because CFr-end^{del} exhibited similar growth to the WT *C. freundii* despite profound defects in NH_4^+ production (Figure S4D), we chose this strain for subsequent SBC (Figure 3N).

We next assessed tumor burden in mice colonized with either WT *C. freundii* or CFr-end^{del} (Figures 3O–3Q). While the WT *C. freundii* promoted MM progression as expected, CFr-end^{del} failed to do so. In addition, after treatment with BTZ, the mice with CFr-end^{del} colonization exhibited significantly lower tumor luminescence intensity (Figures 3O and 3P) and serum IgG2b (Figure 3Q) compared to those with WT *C. freundii* colonization. Cecal and serum concentrations of NH_4^+ were indeed lower in CFr-end^{del}-colonized mice compared with the WT CFr-colonized mice, in either the presence or the absence of BTZ (Figures 3R and 3S).

To determine whether the reduction in NH_4^+ production was responsible for the observed defects of CFr-end^{del} in promoting MM progression and drug resistance, we performed rescue experiments by resupplying NH_4^+. These experiments revealed that tumor luminescence (Figures 3O and 3P) and serum IgG2b (Figure 3Q) were significantly higher in NH_4^+-supplemented BTZ-treated CFr-end^{del} mice compared to mice treated with BTZ alone. The NH_4^+ in cecal contents also correlated positively with those in serum samples of mice under various experimental conditions (Figure 3T), and similar changes were observed in relative abundance of *C. freundii* in feces from the different treatment groups (Figure S4E). We further evaluated the level of NH_4^+ in the bone marrow (BM) of the experimental mice (Figures S4F and S4G). Compared with the PBS group, the level of BM NH_4^+ in the BTZ group was significantly reduced, while BM NH_4^+ in the CFr-WT group was significantly elevated. A higher level of BM NH_4^+ was observed in the CFr+BTZ group than that in the BTZ group, while a lower level of BM NH_4^+ was observed in the CFr-end^{del} group than that in the CFr-WT group. Also, a higher level of BM NH_4^+ was observed in the CFr+BTZ group and in the CFr-end^{del}+BTZ+NH_4Cl group than that in the CFr-end^{del}+BTZ group. These results indicate that the deletion of *end* in *C. freundii* reduces the level of BM NH_4^+ of the experimental mice.

Finally, to determine whether *end* plays a role in the production of NH_4^+, we assessed the expression of the *end* gene in the cecal contents (Figure 3U) and found strong positive correlations between *end* (represented by *end* mRNA levels) and NH_4^+ in both cecal contents and serum (Figure 3V). Together, these results indicate that *C. freundii* produces a large fraction of NH_4^+ by expressing deaminases, and NH_4^+ produced in the intestinal tract subsequently enter the circulation and eventually travel to the BM, causing MM cells to become resistant to BTZ (Figure 3W).

(C and D) Overall (C) and progression-free (D) survival curves of ADs grouped into low- or high-NH_4^+ based on median serum NH_4^+ concentration. Source data are provided in Data S1.
(E) Clonogenic analysis of ARP1 and H929 cells treated with physiological saline, BTZ (6 nM), NH_4Cl (0.5 mM), or NH_4Cl plus BTZ (n = 3 independent experiments).
(F) Statistical analysis of the percentage of apoptotic ARP1 and H929 cells among the eight treatment groups shown in (E) (n = 3 independent experiments).
(G) Schematics of the NH_4Cl gavage experiments in 5TGM1 MM mice.
(H) Live imaging of tumor-associated luminescence intensity in 5TGM1 MM mice treated with physiological saline, BTZ, NH_4Cl, or NH_4Cl plus BTZ.
(I) Serum IgG2b determined via ELISA (n = 4 in each group).
(J and K) NH_4^+ concentrations in cecal contents (J) and serum (K) from 5TGM1 MM mice.
(L) Pearson correlation of NH_4^+ concentrations from cecal contents and serum (n = 16).
(M) Heatmap shows the relative expression of *C. freundii* deaminase in cecal contents from the eight 5TGM1 MM mouse groups shown in Figure 2F.
(N) Schematic of the CFr-end^{del} transplantation experiments of 5TGM1 MM mice.
(O) Live imaging of the tumor-associated luminescence intensity (logarithm) in 5TGM1 MM control mice (PBS), mice treated with CFr-WT transplantation, and mice treated with CFr-end^{del} transplantation, ±BTZ and NH_4Cl.
(P) Quantification of tumor-associated luminescence intensity in the 5TGM1 MM mice cohorts shown in (O).
(Q) Serum IgG2b determined via ELISA (n = 5 in each group).
(R and S) NH_4^+ concentrations in cecal contents (R) and serum (S) from 5TGM1 MM mice.
(T) Pearson correlation of NH_4^+ concentrations from cecal contents and serum (n = 35).
(U) Relative expression of end in cecal contents derived from CFr-end^{del} transplantation experiments of 5TGM1 MM mice.
(V) Pearson correlation of relative expression of end and cecal/serum NH_4^+ concentrations in CFr-end^{del} transplantation experiments (n = 30).
(W) Schematics of *C. freundii* producing ammonium through deaminase and promoting drug resistance to BTZ in MM.
Data represent mean ± SEM in (A), (B), (E), (F), (I)–(K), (P)–(S), and (U). Statistics used paired two-tailed t test (A [right] and B [right]), unpaired two-tailed t test (A [left], B [left], F, I–K, P–S, and U), or log-rank test (C and D).

Table 1. The correlation between fecal NH_4^+ concentration and clinical characteristics in MM

Patients' characteristics	Low NH_4^+ (n = 15; n/N*100%)	High NH_4^+ (n = 16; n/N*100%)	p value
Gender (M/F/NA)	10/5/0	8/6/2	NS
Age (years)	54.87	59.07	NS
BMI (kg/m^2)	23.72	21.36	NS
Heavy chain (g/L)	46.37	43.65	NS
Light chain (g/L)	13.47	9.32	NS
Creatinine (μM)	139.93	60.50	0.0427[a]
Urea (mM)	13.85	4.74	0.0434[a]
Uric acid (mM)	396.77	295.80	0.0345[b]
β2-microglobulin (mg/L)	9.48	3.47	0.0274[a]
Subtype of MM			
IgG	9/15 (60)	8/16 (50)	NS
IgA	2/15 (13.3)	2/16 (12.5)	NS
IgD	1/15 (6.7)	2/16 (12.5)	NS
κ	2/15 (13.3)	1/16 (6.3)	NS
Nonsecretory	1/15 (6.7)	3/16 (18.8)	NS
Plasma cell ratio			
<20%	10/12 (83.3)	10/12 (83.3)	NS
20%–50%	2/12 (16.7)	1/12 (8.3)	NS
>50%	0/12 (0)	1/12 (8.3)	NS
ISS stage			
I	2/10 (20)	1/13 (7.7)	NS
II	3/10 (30)	4/13 (30.8)	NS
III	5/10 (50)	8/13 (61.5)	NS
DS stage			
I	0/10 (0)	0/13 (0)	0.0237[c]
II	4/10 (40)	0/13 (0)	0.0237[c]
III	6/10 (60)	13/13 (100)	0.0237[c]

NS, not significant; F, female; M, male.
[a]p value calculated using two-tailed Wilcoxon rank-sum test
[b]p value calculated using two-tailed Welch's t test
[c]p value calculated using Fisher's exact test

NH_4^+ induces resistance to bortezomib by stabilizing NEK2

Two transporters of NH_4^+ are reportedly coded by the genes *NKCC1* and *NKCC2*.[34,35] We found that only *NKCC1* (alias: *SLC12A2*) was expressed in ARP1 and H929 MM cells (Figure S5A), with expression levels gradually increasing during treatment with NH_4Cl (Figure 4A). Interestingly, compared with healthy donors (HDs), higher SLC12A2 was observed in $CD138^+$ plasma cells sorted from the BM of patients with MM (Figure S5B), and those patients with MM with high SLC12A2 (gene probe 204404_at, GEO: GSE2658) were associated with poor prognosis (Figure 4B).[36] Subsequently, we generated lentivirus containing ARP1-shRNAs (ARP1-SLC12A2-sh1 and -sh2) to deplete *SLC12A2* in ARP1 cells (Figure S5C). SLC12A2 depletion reduced NH_4^+ uptake (Figure 4C), induced apoptosis of ARP1 cells, and almost completely abrogated the inhibitory effect of NH_4^+ on BTZ (Figures 4D and S5D).

In addition, we produced ARP1-Scr and ARP1-SLC12A2sh cells (with luciferase expression) and injected them into NCG mice to simulate an SLC12A2-KO MM mouse model. We then conducted *in vivo* analyses with the SLC12A2-KO mice (Figure S5E). After treating those mice with NH_4^+ and BTZ, we measured tumor luminescence and did not find significant increase in the ARP1-SLC12A2sh+BTZ+NH_4Cl group compared with the ARP1-SLC12A2sh+BTZ group (Figures 4E and 4F), suggesting that SLC12A2 depletion prevents the effects of NH_4Cl treatment on MM in the present BTZ. We detected significantly higher NH_4^+ in cecal contents and serum of the ARP1-SLC12A2sh+BTZ+NH_4Cl mice than those of the ARP1-SLC12A2sh+BTZ mice, demonstrating the efficacy of NH_4Cl treatment (Figures S5F and S5G). Furthermore, while the expression of SLC12A2 and NEK2 could be detected in the BM $CD138^+$ cells sorted from the experimental mice (Figures S5H and S5I), we did not observe significant differences in SLC12A2 and NEK2 between the ARP1-SLC12A2sh+BTZ+NH_4Cl and ARP1-SLC12A2sh+BTZ mice (Figure S5H). In contrast, we observed significant reduction in SLC12A2 and NEK2 in the ARP1-SLC12A2sh+BTZ+NH_4Cl mice compared with the ARP1-Scr+BTZ+NH_4Cl mice (Figure S5I). Thus, SLC12A2 depletion markedly downregulates NEK2 when the experimental mice are exposed to NH_4Cl.

To explore the metabolic fate of NH_4^+ after its uptake, we tracked nitrogen metabolism in ARP1 cells cultured with $^{15}NH_4Cl$ (Figure 4G), finding that most amino acids could be labeled after culturing 12 h (Figure S5J; Table S4). In particular, five amino acids—glycine, alanine, serine, glutamine, and glutamate—were detected to alter after 30 min (Figures 4H, 4I, and S5K). Moreover, we applied ARP1 cells treated with or without NH_4^+ for RNA sequencing (RNA-seq), discovering a few genes with change at the mRNA level, including those in amino acid metabolism, cell cycle, deacetylase, and acetyltransferase (Figure S5L).

How does NH_4^+ confer drug resistance to BTZ? We previously reported that NEK2 is a key chromosomal instability (CIN) gene that can induce drug resistance mainly by activating efflux drug pumps and is associated with poor prognosis in MM.[7] Interestingly, we found that as NH_4^+ treatment progressed, the level of NEK2 protein increased gradually in ARP1 and H929 cells (Figure 4J), while no significant change was observed at the mRNA level (Figure S5M). Similarly, the levels of AURKA and PLK1, both of which are encoded by CIN genes, were also elevated in a time-dependent manner (Figure S5N). The NH_4^+-induced reduction of NEK2 protein in ARP1 and H929 cells led us to ask whether NH_4^+ affects NEK2 protein stability. We therefore treated the cells with NH_4^+ in the presence or absence of cycloheximide (CHX), an inhibitor of protein synthesis. NH_4^+ markedly elevated the level of NEK2 in CHX-treated cells (Figure S5O), suggesting that NH_4^+ functions to stabilize NEK2 protein, thereby inducing an increase in the protein level.

Similarly, we also produced the ARP1-NEK2sh cells and injected them into B-NDG mice to simulate the NEK2-KO MM mouse model (Figure S6A). We did not observe significant differences in the tumor-associated luminescence intensity between the ARP1-NEK2sh+NH_4Cl and the ARP1-NEK2sh mice (Figures S6B and S6C), while both the cecal and serum NH_4^+ were significantly higher in the ARP1-NEK2sh+NH_4Cl mice

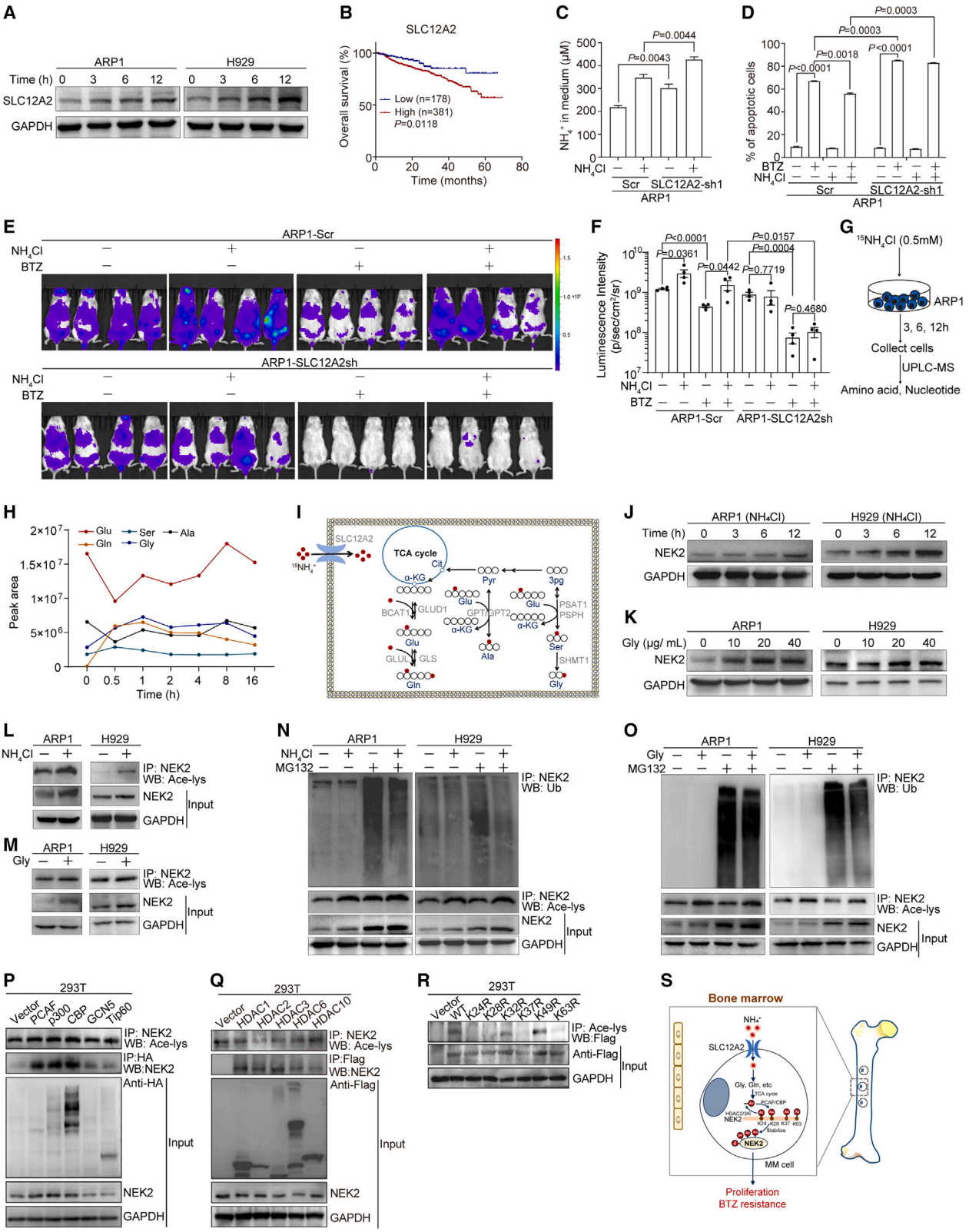

Figure 4. Ammonium induces resistance to bortezomib by stabilizing NEK2 expression

(A) Western blotting of SLC12A2 and GAPDH in ARP1 and H929 cells cultured with NH_4Cl for 0, 3, 6, or 12 h. Source data are provided in Data S1.

(B) Overall survival curves of patients with MM grouped based on low or high expression of SLC12A2. Source data are provided in Data S1.

(legend continued on next page)

than the ARP1-NEK2sh mice (Figures S6D and S6E). Furthermore, a positive correlation between the cecal and serum NH_4^+ levels was observed (Figure S6F). We next examined the expression of SLC12A2 and NEK2 in the BM CD138+ cells sorted from the experimental mice and detected significantly higher SLC12A2 levels in the ARP1-NEK2sh+NH_4Cl mice than the ARP1-NEK2sh mice, while little changes in NEK2 were seen between the two groups (Figure S6G). These results indicate that both SLC12A2 and NEK2 are indispensable for promoting progression in MM and inducing MM resistance to BTZ.

NH_4^+ enhances NEK2 acetylation while reducing NEK2 ubiquitination

To explore potential downstream effector(s) of NH_4^+ in the regulation of drug resistance in MM, we examined the potential role of glycine for the following reasons: first, we previously reported that glycine can promote MM proliferation and drug resistance[10]; second, we found earlier in this study that NH_4^+, when supplied in the culture medium, can be incorporated into a variety of amino acids including glycine and glutamine. We therefore treated ARP1 and H929 cells with a range of glycine or glutamine concentrations and found that NEK2 was gradually upregulated with increasing doses of glycine or glutamine (Figures 4K and S6H).

It has been shown that, in mammalian cells, amino acids may control protein functions at the level of post-translational modifications, including protein acetylation, phosphorylation, and ubiquitination.[37] To examine whether NH_4Cl/glycine/glutamine can modulate NEK2 post-translationally, we treated ARP1 and H929 cells with NH_4Cl or glycine or glutamine, finding that the levels of total and acetylated NEK2 were elevated upon NH_4Cl/glycine/glutamine treatment (Figures 4L, 4M, S6I, and S6J). Because NEK2 is mainly degraded through the proteasome pathway,[26] we further assessed the ubiquitination of NEK2 after NH_4Cl/glycine/glutamine treatment. Treatment with MG132, a proteosome inhibitor, caused an increase in ubiquitinated NEK2, while NH_4Cl/glycine/glutamine treatment markedly attenuated this increase in NEK2 ubiquitination. In contrast, the level of acetylated NEK2 was elevated after NH_4^+ treatment when compared with MG132 treatment alone (Figures 4N, 4O, and S6J).

Protein acetylation is mainly regulated by acetyltransferases and deacetylases. To explore which acetyltransferases regulate NEK2 acetylation, we conducted several *in vitro* experiments (Figure S6K). Therein, after treating MM cells (ARP1 and H929) with NH_4Cl/glycine/glutamine, we detected significantly higher levels of acetyl-CoA (Figure S6L). In addition, we individually transfected 5 acetyltransferases using pCDNA3.1-HA-PCAF, pCDNA3.1-HA-p300, pCDNA3.1-HA-CBP, pCDNA3.1-HA-GCN5, and pCDNA3.1-HA-Tip60 into HEK293T cells. We found that NEK2 and Ace-NEK2 were enhanced only after over-expressing PCAF, p300, and CBP, and simultaneously strong binding of PCAF, p300, and CBP proteins to NEK2 was seen (Figure 4P). We then treated ARP1 and H929 cells with NH_4^+, SIRT inhibitors (NAM), or HDAC inhibitors (TSA). Notably, we observed an increase in NEK2 and Ace-NEK2 following TSA treatment (Figure S6M), suggesting that HDAC family members predominantly regulate the deacetylation of NEK2. Subsequently, we transfected HEK293T cells with 5 deacetylases using pCDNA3.1-Flag-HDAC1, pCDNA3.1-Flag-HDAC2, pCDNA3.1-Flag-HDAC3, pCDNA3.1-Flag-HDAC6, and pCDNA3.1-Flag-HDAC10, revealing that HDAC1, 2, 3, 6, and 10 all bind to NEK2, with HDAC2, HDAC3, and HDAC6 being the primary regulators of NEK2 deacetylation (Figure 4Q). To further validate the roles of these identified deacetylases and acetyltransferases, we treated ARP1 and H929 cells with NH_4Cl. This treatment resulted in the downregulation of HDAC2, HDAC3, and HDAC6, as well as the upregulation of PCAF and CBP (Figure S6N). These findings support the notion that NH_4^+ primarily modulates NEK2 acetylation through downregulating HDAC2, HDAC3, and HDAC6 and upregulating PCAF and CBP (Figure 4Q). Furthermore, six lysine residues (K24, K28, K32, K37, K49, and K63) were identified in the conserved sequences of the human NEK2 protein, allowing us to identify these potential specific acetylation sites on NEK2. To pinpoint these acetylation sites, we mutated these lysine residues individually to arginine (simulating deacetylation)

(C) NH_4^+ concentrations in the culture medium of ARP1 cells expressing control (scrambled, Scr) or SLC12A2-targeting (SLC12A2-sh1) shRNA, with or without NH_4Cl.
(D) Statistical analysis of the percentage of apoptotic Scr or SLC12A2-sh1 ARP1 cells treated with or without NH_4Cl and BTZ.
(E) Live imaging of the tumor-associated luminescence intensity in NCG MM mice treated with 0.9% NaCl, BTZ (0.75 mg/kg once/2 days), NH_4Cl (5.35 mg/mL every day), or NH_4Cl plus BTZ.
(F) Quantification of tumor-associated luminescence intensity in the NCG MM mice cohorts shown in (E).
(G) Schematics of the NH_4Cl metabolic flux experiments.
(H) Targeted metabolomics assays of glutamate (Glu), glutamine (Gln), glycine (Gly), serine (Ser), and alanine (Ala) in ARP1 cells supplemented with NH_4Cl (0.5 mM).
(I) Schematics of NH_4Cl metabolism in MM cells.
(J) Western blotting of NEK2 and GAPDH in ARP1 and H929 cells cultured with NH_4Cl for 0, 3, 6, or 12 h. Source data are provided in Data S1.
(K) Western blotting of NEK2 and GAPDH in ARP1 and H929 cells cultured with or without Gly for 12 h. Source data are provided in Data S1.
(L) Acetylation of endogenous NEK2 in ARP1 and H929 cells treated with or without NH_4Cl. NEK2 acetylation was analyzed by using immunoprecipitation with an anti-acetyl-lys antibody followed by western blotting for NEK2.
(M) Acetylation of endogenous NEK2 in ARP1 and H929 cells treated with or without Gly.
(N) Acetylation and ubiquitylation of endogenous NEK2 in ARP1 and H929 cells treated with or without NH_4Cl and MG132.
(O) Acetylation and ubiquitylation of endogenous NEK2 in ARP1 and H929 cells treated with or without Gly and MG132.
(P) Co-precipitation of endogenous NEK2 and acetylated NEK2 with each of the indicated HA-tagged acetyltransferase from HEK293T cells.
(Q) Co-precipitation of endogenous NEK2 and acetylated NEK2 with each of the indicated Flag-tagged deacetylases from HEK293T cells.
(R) Acetylation of NEK2 mutants expressed in HEK293T cells. Source data are provided in Data S1.
(S) Schematics of our working hypothesis for the mechanism by which NH_4^+ promotes MM cell proliferation.
Data represent mean ± SEM in (C) and (D). Statistics were calculated via log rank test (B) or unpaired two-tailed t test (C and D).

CellPress
OPEN ACCESS

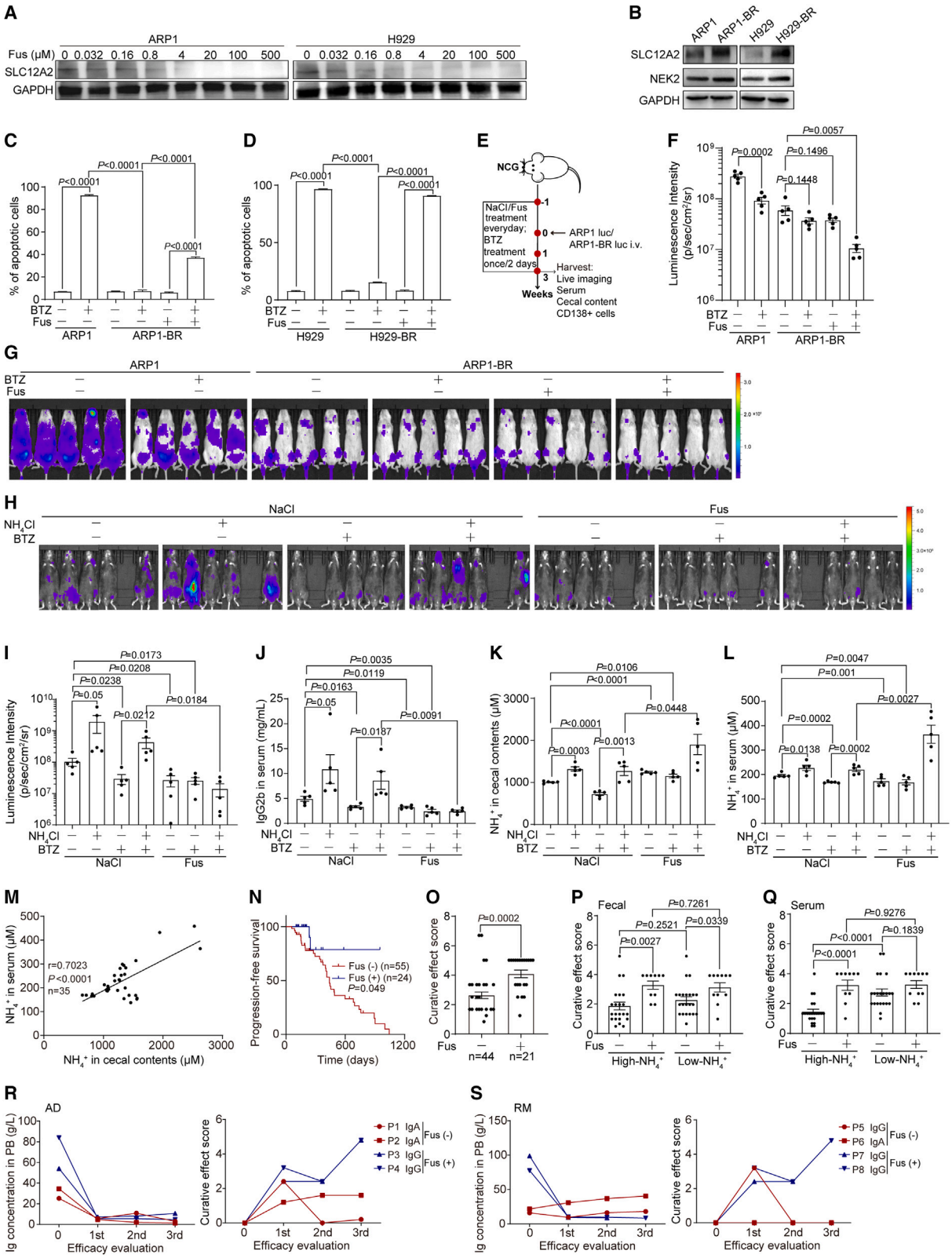

Figure 5. Inhibition of ammonium intake by furosemide sodium reduces bortezomib resistance

(A) Western blotting of SLC12A2 and GAPDH in ARP1 and H929 cells cultured with or without Fus for 48 h.

(B) Western blotting of SLC12A2 and GAPDH in WT and bortezomib (BTZ)-resistant (BR) ARP1 and H929 cells.

(legend continued on next page)

and then ligated the mutated genes into PCDH-GFP lentiviral vectors to infect HEK293T cells. We found that all these mutants, K24R, K28R, K37R, and K63R, led to decreased acetylation of exogenous NEK2, indicating that these are the bona fide acetylation sites on NEK2 (Figure 4R). Together, these results indicate that NH_4^+ can be incorporated into a variety of amino acids that enhance the acetylation of NEK2 while reducing its ubiquitination and subsequently attenuating its degradation, leading to reduced apoptosis of MM cells (Figure 4S).

Inhibition of NH_4^+ intake by furosemide sodium restores BTZ resistance in MM cells

Having identified SLC12A2 as the key transmembrane transporter that mediates the uptake of NH_4^+ by MM cells, we explored the therapeutic potential of targeting SLC12A2 in MM relapse. Interestingly, we came across furosemide sodium (Fus), which was originally utilized in our practice to manage volume load and prevent heart and renal failure in patients with MM, based on previously documented benefit of Fus in a small number of patients with MM with renal failure.[38] Fus is an established loop diuretic that promotes the passage of salt into urine and prevents Na,K-ATPase activation in rat cardiac fibroblasts, thus preventing the body from absorbing too much salt.[39] Surprisingly, we observed significant favorable clinical outcomes in patients with MM who received Fus treatment. We discovered that Fus can downregulate the expression of SLC12A2 in ARP1 and H929 cells in a dose-dependent manner (Figure 5A). Additionally, as previously described, we established three drug resistance cell lines, including ARP1-BR and H929-BR.[7,40] Consistent with the role of SLC12A2 in BTZ resistance, we detected higher expression of SLC12A2 in these three BTZ-resistant cells than in the WT cells (Figure 5B). We therefore tested whether Fus could restore drug susceptibility to BTZ-resistant ARP1 and H929 cells. Indeed, the addition of Fus significantly enhanced apoptosis in BTZ-treated drug-resistant cells (Figures 5C, 5D, S7A, and S7B), indicating that, by downregulating SLC12A2, Fus might have potential as a therapeutic reagent to increase BTZ susceptibility in MM cells.

We then extended our analysis of Fus to MM animal models *in vivo* using BTZ-resistant ARP1 cells (ARP1-BR) (Figure 5E). We conducted live imaging of those experimental mice (Figures 5F and 5G). When comparing luminescence intensity between the ARP1-BR group and the ARP1-BR+BTZ group, we noted an insignificant decrease in luminescence in the latter group. However, a significant decrease was observed in the ARP1-BR+BTZ+Fus group (Figure 5H). Additionally, when comparing the ARP1-BR+BTZ group to the ARP1-BR+BTZ+Fus group, we detected significantly lower levels of serum and cecal NH_4^+ in the ARP1-BR+BTZ+Fus group (Figures S7C and S7D). Furthermore, we found downregulated NEK2 and SLC12A2 expression in CD138+ cells derived from the BM of the experimental mice in the ARP1-BR+BTZ+Fus group (Figure S7E).

Continuing our investigation of Fus in MM animal models *in vivo*, we utilized models constructed using 5TGM1 cells (Figure S7F) and assessed tumor burden in experimental mice with or without Fus treatments. While the addition of NH_4Cl reversed the effect of BTZ on tumor burden, as manifested by a reduction in serum IgG2b and tumor luminescence intensity, Fus almost completely abolished this adverse effect of NH_4Cl (Figures 5H–5J). The effect of Fus was not due to an overall reduction of NH_4^+; NH_4^+ levels were in fact consistently higher in Fus-treated mice compared to control mice (Figures 5K and 5L), likely due to the inability of NH_4^+ to enter the SLC12A2-depleted cells. In addition, the concentrations of NH_4^+ in cecal contents and serum samples from mice with various treatments correlated positively (Figure 5M). We also assessed SLC12A2 expression in the intestine and tibia of representative mice via immunocytochemistry and found that Fus treatment effectively reduced the level of SLC12A2, as in our *in vitro* experiments (Figure S7G). Furthermore, we performed *in vivo* testing on MM cells treated with NH_4^+ in combination with Fus treatment (Figure S7H). The results showed a significantly decreased luminescence intensity of the NH_4Cl+Fus group compared with the NH_4Cl group (Figures S7I and S7J). Simultaneously, we detected a significant increase in cecal NH_4^+ levels and a decrease in serum NH_4^+ levels in the NH_4Cl+Fus group compared with the NH_4Cl group (Figures S7K and S7L). In addition, we further evaluated the level of NH_4^+ in the BM of the experimental mice and consistently found lower NH_4^+ levels in the NH_4Cl+Fus group compared with the NH_4Cl group (Figures S7M and S7N). Thus, Fus suppresses the serum and BM NH_4^+ levels and downregulates ammonium uptake in MM cells, ultimately reducing the BTZ resistance-promoting effects associated with NH_4Cl supplementation *in vivo*.

(C and D) Statistical analysis of the percentage of apoptotic ARP1 and ARP1-BR cells (C) or H929 and H929-BR cells (D) treated with or without BTZ (10 nM) and furosemide sodium (Fus; 4 μM).
(E) Schematics of the *in vivo* experiments in NCG mice injected with luciferase-expressing ARP1 and ARP1-BR cells to induce MM.
(F) Quantification of tumor-associated luminescence intensity in NCG MM mice.
(G) Live imaging of the tumor-associated luminescence intensity in NCG MM mice treated with physiological saline, BTZ (0.75 mg/kg once/2 days), Fus (10 mg/kg every day), or Fus plus BTZ.
(H) Live imaging of tumor-associated luminescence intensity in 5TGM1 MM mice treated with physiological saline (NaCl), NH_4Cl (5.35 mg/mL once per day), BTZ, Fus (10 mg/kg once per day), or combinations of NH_4Cl, BTZ, and/or Fus.
(I) Quantification of tumor-associated luminescence intensity in the 5TGM1 MM mice cohorts shown in (H).
(J) Concentrations of IgG2b in mouse serum as detected with ELISA (n = 5 in each group).
(K and L) NH_4^+ concentrations in cecal contents (K) and serum (L) from 5TGM1 MM mice.
(M) Pearson correlation of NH_4^+ concentrations from cecal contents and serum (n = 35).
(N) Progression-free survival curves of patients with MM treated with or without Fus. Source data are provided in Data S1.
(O) Curative effect score in patients with MM treated with or without Fus.
(P and Q) Curative effect score in patients with MM treated with or without Fus and grouped by low or high NH_4^+ in fecal contents (P) or serum (Q).
(R) Peripheral blood (PB) Ig concentrations and curative effect scores in representative high-NH_4^+ ADs treated with or without Fus.
(S) PB Ig concentrations and curative effect scores in representative high-NH_4^+ RMs treated with or without Fus.
Data represent mean ± SEM in (C), (D), (F), (I)–(L), and (O)–(Q). Statistics were calculated via unpaired two-tailed t test (C, D, F, I–L, and O–Q), or log-rank test (M).

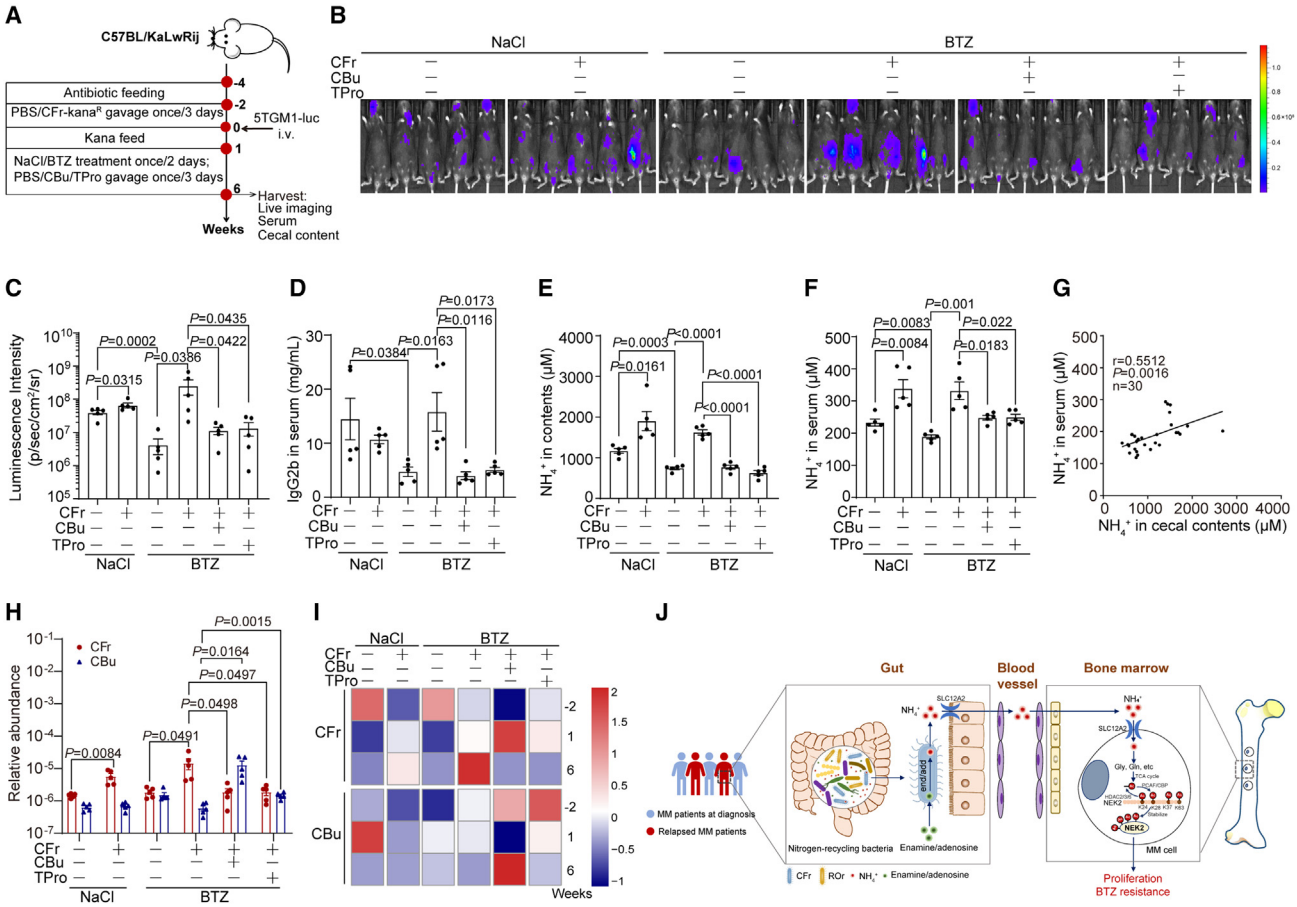

Figure 6. Probiotic supplementation reduces bortezomib resistance of MM

(A) Schematics of the *in vivo* experiments.

(B) Live imaging of the tumor-associated luminescence intensity in 5TGM1 MM mice treated with PBS or the indicated combinations of BTZ and *C. freundii*, *C. butyricum*, or TPro transplantation in week 4.

(C) Quantification of tumor-associated luminescence intensity in the 5TGM1 MM mice cohorts shown in (B).

(D) Concentrations of IgG2b in mouse serum as detected with ELISA (n = 5 in each group) in week 6.

(E and F) NH_4^+ concentrations in cecal contents (E) and serum (F) from 5TGM1 MM mice.

(G) Correlation of NH_4^+ concentrations from cecal contents and serum (n = 30).

(H) Relative abundance of *C. freundii* and *C. butyricum* in fecal samples derived from 5TGM1 MM mice.

(I) Heatmap showing the relative abundance of *C. freundii* and *C. butyricum* in fecal samples from the indicated 5TGM1 MM mice at −2, 1, and 6 weeks.

(J) Schematics of our working hypothesis.

Data represent mean ± SEM in (C)–(F) and (H). Statistics were calculated via unpaired two-tailed t test (C–F and H) or two-tailed Pearson correlation analysis (G).

Finally, we analyzed the effect of Fus treatment in patients with MM (Table S5). We found that the patients with MM treated with Fus achieved longer progression-free survival (Figure 5N; Table S6) and higher curative effect scores (Figure 5O; Table S6). In particular, when the clinical cases were divided into high- and low-NH_4^+ groups based on the median fecal NH_4^+ concentration, we observed much higher curative effect scores in those patients with Fus treatment (Figure 5P; Table S6). Similar results were also obtained in the high-NH_4^+ group when the clinical cases were divided into high- and low-NH_4^+ groups based on the median serum NH_4^+ concentration (Figure 5Q; Table S6). Next, we selected four ADs with high fecal and serum NH_4^+ concentrations, including two patients with and two patients without Fus treatment, for more detailed analyses. We observed a profound reduction in Ig concentration in PB and higher curative effect scores in patients with Fus treatment (Figure 5R; Table S6). Similarly, RMs with Fus treatment also exhibited much better clinical outcomes (Figure 5S; Table S6).

Probiotic supplementation reduces BTZ resistance of MM

To explore additional strategies for tackling drug resistance in MM, we tested the possibility of *Clostridium butyricum* (*C. butyricum*), which was previously described.[18] We performed single *C. butyricum* and triple probiotic (TPro; i.e., *Clostridium butyricum*, *Bacillus mesentericus*, and *Streptococcus faecalis*) colonization by gavage (Figure 6A). As previously observed, tumor-associated luminescence intensity and serum IgG2b in CFr+BTZ mice were significantly higher than in BTZ mice, but these markers were also significantly reduced in CFr mice

treated with *C. butyricum* or TPro supplementation (Figures 6B–6D). While the concentrations of NH_4^+ in cecal contents and serum samples from CFr and CFr+BTZ mice were higher than in the control mice, they were much lower in CFr+BTZ+CBu and CFr+BTZ+TPro mice than in the CFr+BTZ mice, in keeping with the results of the tumor burden analysis (Figures 6E and 6F). We also assessed the concentration of NH_4^+ in cecal contents and serum samples of all experimental mice and found a positive correlation (Figure 6G).

Next, to determine how *C. butyricum* might cross-modulate *C. freundii* to influence NH_4^+ production, we assessed *C. freundii* abundance in mouse feces before and after *C. butyricum* transplantation. We found that *C. butyricum* transplantation markedly reduced *C. freundii* abundance (Figures 6H and 6I), suggesting that *C. butyricum* inhibits the growth of *C. freundii*, a representative of nitrogen-recycling bacteria, thereby decreasing NH_4^+ production and alleviating the resistance of MM cells to BTZ. In keeping with the effect of *C. butyricum* transplantation, TPro, a CFDA-approved clinical drug, exhibited consistent efficacy in alleviating BTZ resistance.

DISCUSSION

MM drug resistance involves a complex interplay between genetic and microenvironmental factors. Our study reveals an imbalance in nitrogen-recycling bacteria and, specifically, *C. freundii* in relapsed MM patients. We established a critical role for *C. freundii* in inducing BTZ resistance. Mechanistically, ammonium produced by *C. freundii* enters MM cells through SLC12A2, contributing to amino acid synthesis and acetyl-CoA production for NEK2 protein modification. Fus downregulates SLC12A2, improving outcomes (Figure 6J). This novel insight unveils *C. freundii* and ammonium as key MM relapse modulators, providing new therapeutic targets for MM progression and drug resistance.

Key factors contributing to MM treatment failure include the evolution of tumor initiation cells, signal pathway abnormalities due to genetic alterations, and aberrant interactions with the BMME. Our previous study identified a unique amino acid metabolic imbalance in the BMME, driven by MMP13-mediated degradation of bone collagen.[10] This imbalance promotes MM development, with glycine inducing cell proliferation via glutathione synthesis and excessive serine impairing megakaryopoiesis.[41] Enriched amino acids are decomposed into urea, providing nitrogen for bacteria like *C. freundii* and *R. ornithinolytica*.[18] Our present study uncovers a group of nitrogen-recycling bacteria, including *C. freundii*, and establishes their causal role in MM drug resistance. Specifically, *C. freundii* enriched in relapsed patients with poor responses to BTZ treatment is linked to deaminase expression, ammonium production, and effects on MM cell proliferation and apoptosis. These findings offer new insights into the molecular mechanism and intestinal microbial homeostasis governing MM drug resistance.

Prior studies have demonstrated that intestinal microorganisms can induce drug resistance in cancer cells through various mechanisms.[13,17,42] This study focuses on *C. freundii*, revealing its indirect induction of drug resistance through a crucial signaling intermediate—ammonium. Elevated circulating ammonium can damage organs and cells, impacting synthesis processes and activating oxidative stress-related signaling pathways.[43–48] Patients with higher ammonium exhibit poorer prognosis.[45,49] Mechanistically, ammonium is transported into MM cells via SLC12A2/NKCC1 protein transporter, contributing to the synthesis of non-essential amino acids.

The lack of early detection markers and effective interventions contributes significantly to MM drug resistance. Our findings demonstrate that ammonium is a potential dual-purpose tool for early detection and therapeutic targeting. Several previous studies reported ornithine and spironolactone for ammonia elimination.[39,50,51] We discovered that Fus, known for inhibiting Na,K-ATPase, downregulates SLC12A2, reducing ammonium uptake in MM cells.[34] Fus treatment is associated with improved outcomes, especially in high-ammonium patient groups, suggesting a promising therapeutic strategy for MM relapse.

Finally, in keeping with the effects of Fus administration, we find that the probiotics TPro and *C. butyricum* alleviate MM cell resistance to BTZ by re-balancing intestinal flora and reducing NH_4^+ production. Future research should explore the effectiveness of Fus in a larger clinical context, deciphering its mechanism of downregulating SLC12A2 and assessing the potential for treating various hyperammonemic disorders.

Limitations of the study

This study had several limitations, including the limited number of metagenomics sequencing samples and MM patients treated with Fus. The single-center focus suggests the need for broader representation from multiple centers in the future. Additionally, a lack of systematic exploration of various factors in sequential samples and the need for further clinical studies on Fus and probiotics for MM cell resistance to BTZ are noted limitations.

STAR★METHODS

Detailed methods are provided in the online version of this paper and include the following:

- KEY RESOURCES TABLE
- RESOURCE AVAILABILITY
  - Lead contact
  - Materials availability
  - Data and code availability
- EXPERIMENTAL MODEL AND SUBJECT DETAILS
  - Mice
  - Patients and clinical samples
  - Human survival analysis
  - Cell lines
- METHOD DETAILS
  - Metagenomic sequencing and taxonomic classification
  - Real-time quantitative PCR (qPCR)
  - Bacterial diversity
  - Mouse xenograft models of MM
  - Fecal microbiota transplantation
  - Bacterial fluid colonization
  - Ammonium transplantation experiment and sample collection
  - Experiment of furosemide sodium-assisted BTZ in the treatment of MM

- ARP1-NEK2sh experiment and sample collection
- ARP1-SLC12A2sh experiment and sample collection
- Experiment of furosemide sodium-assisted BTZ in the treatment of MM-BR
- Construction of deaminase-deletion *Citrobacter freundii*
- Nessler's staining of biological tissues
- Immunocytochemistry
- Western blotting
- Acetyl CoA assay
- Soft agar clonogenicity assay
- Vectors, transfections, and transductions
- Ammonia tracing
- RNAseq and quantitative analysis
- Flow cytometry
- Immunoprecipitation

● QUANTIFICATION AND STATISTICAL ANALYSIS

SUPPLEMENTAL INFORMATION

Supplemental information can be found online at https://doi.org/10.1016/j.cmet.2023.11.019.

ACKNOWLEDGMENTS

The authors thank Professor Rushi Liu and Kaiqun Ren from Hunan Normal University School of Medicine for technical assistance. Thanks to the Animal Center of Hunan Normal University School of Medicine for providing the experimental platform. W.Z., Y.H., and X.J. are supported by the National Natural Science Foundation of China under award numbers 82130006, 81974010, 82170202, and 32370062; Haihe Laboratory of Cell Ecosystem Innovation Fund under award number 22HHXBSS00030; SKLEH-Pilot Research Grant under award number ZK22-06; and the Scientific Research Program of Furong Laboratory under award number 2023SK2085-2. X.J. is supported by the National Natural Science Foundation of Hunan Province under award number 2021JJ40995. Yinghong Zhu is supported by the Fundamental Research Fund for Graduate of Central South University under award number 2022ZZTS0225.

AUTHOR CONTRIBUTIONS

W.Z., W.J., and Y.H. designed experiments. Yinghong Zhu, Q.Y., J.Z., J.G., C.H., R.Z., N.H., F.S., J.W., S.H., and Z.L. performed most of the immunohistochemistry, flow cytometry, and other experiments. X.J. and L.X. performed all bioinformatics analyses. Yinghong Zhu and X.J. analyzed data. S.C., G.A., D.J., J.H., Q.Y., X.L., Yan Zhu, L.Z., Y.J., J.L., Xun Chen, and L.Q. led the collection of surgical specimens and related clinical data. W.Z., W.J., Yinghong Zhu, and X.J. wrote the original draft. W.Z., W.J., and Xiang Chen edited the manuscript.

DECLARATION OF INTERESTS

The authors declare no competing interests.

Received: April 10, 2023
Revised: October 17, 2023
Accepted: November 30, 2023
Published: December 18, 2023

REFERENCES

1. Röllig, C., Knop, S., and Bornhäuser, M. (2015). Multiple myeloma. Lancet *385*, 2197–2208.
2. Brody, H. (2011). Multiple myeloma. Nature *480*, S33.
3. Medical Masterclass contributors, and Firth, J. (2019). Haematology: multiple myeloma. Clin. Med. *19*, 58–60.
4. Kyle, R.A., Gertz, M.A., Witzig, T.E., Lust, J.A., Lacy, M.Q., Dispenzieri, A., Fonseca, R., Rajkumar, S.V., Offord, J.R., Larson, D.R., et al. (2003). Review of 1027 patients with newly diagnosed multiple myeloma. Mayo Clin. Proc. *78*, 21–33.
5. Mutlu, P., Kiraz, Y., Gündüz, U., and Baran, Y. (2015). An update on molecular biology and drug resistance mechanisms of multiple myeloma. Crit. Rev. Oncol. Hematol. *96*, 413–424.
6. Kuang, C., Zhu, Y., Guan, Y., Xia, J., Ouyang, J., Liu, G., Hao, M., Liu, J., Guo, J., Zhang, W., et al. (2021). COX2 confers bone marrow stromal cells to promoting TNFalpha/TNFR1beta-mediated myeloma cell growth and adhesion. Cell. Oncol. *44*, 643–659.
7. Zhou, W., Yang, Y., Xia, J., Wang, H., Salama, M.E., Xiong, W., Xu, H., Shetty, S., Chen, T., Zeng, Z., et al. (2013). NEK2 induces drug resistance mainly through activation of efflux drug pumps and is associated with poor prognosis in myeloma and other cancers. Cancer Cell *23*, 48–62.
8. Feng, X., Guo, J., An, G., Wu, Y., Liu, Z., Meng, B., He, N., Zhao, X., Chen, S., Zhu, Y., et al. (2022). Genetic aberrations and interaction of NEK2 and TP53 accelerate aggressiveness of multiple myeloma. Adv. Sci. *9*, e2104491.
9. Yang, Y., Zhou, W., Xia, J., Gu, Z., Wendlandt, E., Zhan, X., Janz, S., Tricot, G., and Zhan, F. (2014). NEK2 mediates ALDH1A1-dependent drug resistance in multiple myeloma. Oncotarget *5*, 11986–11997.
10. Xia, J., Zhang, J., Wu, X., Du, W., Zhu, Y., Liu, X., Liu, Z., Meng, B., Guo, J., Yang, Q., et al. (2022). Blocking glycine utilization inhibits multiple myeloma progression by disrupting glutathione balance. Nat. Commun. *13*, 4007.
11. He, Y., Fu, L., Li, Y., Wang, W., Gong, M., Zhang, J., Dong, X., Huang, J., Wang, Q., Mackay, C.R., et al. (2021). Gut microbial metabolites facilitate anticancer therapy efficacy by modulating cytotoxic CD8(+) T cell immunity. Cell Metab. *33*, 988–1000.e7.
12. Teng, H., Wang, Y., Sui, X., Fan, J., Li, S., Lei, X., Shi, C., Sun, W., Song, M., Wang, H., et al. (2023). Gut microbiota-mediated nucleotide synthesis attenuates the response to neoadjuvant chemoradiotherapy in rectal cancer. Cancer Cell *41*, 124–138.e6.
13. Yu, T., Guo, F., Yu, Y., Sun, T., Ma, D., Han, J., Qian, Y., Kryczek, I., Sun, D., Nagarsheth, N., et al. (2017). Fusobacterium nucleatum promotes chemoresistance to colorectal cancer by modulating autophagy. Cell *170*, 548–563.e16.
14. Bao, Y., Zhai, J., Chen, H., Wong, C.C., Liang, C., Ding, Y., Huang, D., Gou, H., Chen, D., Pan, Y., et al. (2023). Targeting m(6)A reader YTHDF1 augments antitumour immunity and boosts anti-PD-1 efficacy in colorectal cancer. Gut *72*, 1497–1509.
15. Chrysostomou, D., Roberts, L.A., Marchesi, J.R., and Kinross, J.M. (2023). Gut microbiota modulation of efficacy and toxicity of cancer chemotherapy and immunotherapy. Gastroenterology *164*, 198–213.
16. Calcinotto, A., Brevi, A., Chesi, M., Ferrarese, R., Garcia Perez, L., Grioni, M., Kumar, S., Garbitt, V.M., Sharik, M.E., Henderson, K.J., et al. (2018). Microbiota-driven interleukin-17-producing cells and eosinophils synergize to accelerate multiple myeloma progression. Nat. Commun. *9*, 4832.
17. Pianko, M.J., Devlin, S.M., Littmann, E.R., Chansakul, A., Mastey, D., Salcedo, M., Fontana, E., Ling, L., Tavitian, E., Slingerland, J.B., et al. (2019). Minimal residual disease negativity in multiple myeloma is associated with intestinal microbiota composition. Blood Adv. *3*, 2040–2044.
18. Jian, X., Zhu, Y., Ouyang, J., Wang, Y., Lei, Q., Xia, J., Guan, Y., Zhang, J., Guo, J., He, Y., et al. (2020). Alterations of gut microbiome accelerate multiple myeloma progression by increasing the relative abundances of nitrogen-recycling bacteria. Microbiome *8*, 74.
19. Wang, Y., Yang, Q., Zhu, Y., Jian, X., Guo, J., Zhang, J., Kuang, C., Feng, X., An, G., Qiu, L., et al. (2022). Intestinal Klebsiella pneumoniae contributes to pneumonia by synthesizing glutamine in multiple myeloma. Cancers *14*, 4188.

20. Oerlemans, R., Franke, N.E., Assaraf, Y.G., Cloos, J., van Zantwijk, I., Berkers, C.R., Scheffer, G.L., Debipersad, K., Vojtekova, K., Lemos, C., et al. (2008). Molecular basis of bortezomib resistance: proteasome subunit beta5 (PSMB5) gene mutation and overexpression of PSMB5 protein. Blood *112*, 2489–2499.

21. Daniel, K.G., Kuhn, D.J., Kazi, A., and Dou, Q.P. (2005). Anti-angiogenic and anti-tumor properties of proteasome inhibitors. Curr. Cancer Drug Targets *5*, 529–541.

22. de Wilt, L.H.A.M., Jansen, G., Assaraf, Y.G., van Meerloo, J., Cloos, J., Schimmer, A.D., Chan, E.T., Kirk, C.J., Peters, G.J., and Kruyt, F.A.E. (2012). Proteasome-based mechanisms of intrinsic and acquired bortezomib resistance in non-small cell lung cancer. Biochem. Pharmacol. *83*, 207–217.

23. Franke, N.E., Niewerth, D., Assaraf, Y.G., van Meerloo, J., Vojtekova, K., van Zantwijk, C.H., Zweegman, S., Chan, E.T., Kirk, C.J., Geerke, D.P., et al. (2012). Impaired bortezomib binding to mutant beta5 subunit of the proteasome is the underlying basis for bortezomib resistance in leukemia cells. Leukemia *26*, 757–768.

24. Lü, S., and Wang, J. (2013). The resistance mechanisms of proteasome inhibitor bortezomib. Biomark. Res. *1*, 13.

25. Desantis, V., Saltarella, I., Lamanuzzi, A., Mariggiò, M.A., Racanelli, V., Vacca, A., and Frassanito, M.A. (2018). Autophagy: a new mechanism of prosurvival and drug resistance in multiple myeloma. Transl. Oncol. *11*, 1350–1357.

26. Xia, J., He, Y., Meng, B., Chen, S., Zhang, J., Wu, X., Zhu, Y., Shen, Y., Feng, X., Guan, Y., et al. (2020). NEK2 induces autophagy-mediated bortezomib resistance by stabilizing Beclin-1 in multiple myeloma. Mol. Oncol. *14*, 763–778.

27. Saavedra-García, P., Martini, F., and Auner, H.W. (2020). Proteasome inhibition in multiple myeloma: lessons for other cancers. Am. J. Physiol. Cell Physiol. *318*, C451–C462.

28. Tibullo, D., Giallongo, C., Romano, A., Vicario, N., Barbato, A., Puglisi, F., Parenti, R., Amorini, A.M., Wissam Saab, M., Tavazzi, B., et al. (2020). Mitochondrial functions, energy metabolism and protein glycosylation are interconnected processes mediating resistance to bortezomib in multiple myeloma cells. Biomolecules *10*, 696.

29. Zaal, E.A., Wu, W., Jansen, G., Zweegman, S., Cloos, J., and Berkers, C.R. (2017). Bortezomib resistance in multiple myeloma is associated with increased serine synthesis. Cancer Metab. *5*, 7.

30. Wu, X., Xia, J., Zhang, J., Zhu, Y., Wu, Y., Guo, J., Chen, S., Lei, Q., Meng, B., Kuang, C., et al. (2020). Phosphoglycerate dehydrogenase promotes proliferation and bortezomib resistance through increasing reduced glutathione synthesis in multiple myeloma. Br. J. Haematol. *190*, 52–66.

31. Sharma, A., Nair, R., Achreja, A., Mittal, A., Gupta, P., Balakrishnan, K., Edgar, C.L., Animasahun, O., Dwivedi, B., Barwick, B.G., et al. (2022). Therapeutic implications of mitochondrial stress-induced proteasome inhibitor resistance in multiple myeloma. Sci. Adv. *8*, eabq5575.

32. Tsvetkov, P., Detappe, A., Cai, K., Keys, H.R., Brune, Z., Ying, W., Thiru, P., Reidy, M., Kugener, G., Rossen, J., et al. (2019). Mitochondrial metabolism promotes adaptation to proteotoxic stress. Nat. Chem. Biol. *15*, 681–689.

33. Bolzoni, M., Chiu, M., Accardi, F., Vescovini, R., Airoldi, I., Storti, P., Todoerti, K., Agnelli, L., Missale, G., Andreoli, R., et al. (2016). Dependence on glutamine uptake and glutamine addiction characterize myeloma cells: a new attractive target. Blood *128*, 667–679.

34. Hertz, L., Peng, L., and Song, D. (2015). Ammonia, like K(+), stimulates the Na(+), K(+), 2 Cl(-) cotransporter NKCC1 and the Na(+),K(+)-ATPase and interacts with endogenous ouabain in astrocytes. Neurochem. Res. *40*, 241–257.

35. Amlal, H., Paillard, M., and Bichara, M. (1994). NH4+ transport pathways in cells of medullary thick ascending limb of rat kidney. NH4+ conductance and K+/NH4+(H+) antiport. J. Biol. Chem. *269*, 21962–21971.

36. Zhan, F., Huang, Y., Colla, S., Stewart, J.P., Hanamura, I., Gupta, S., Epstein, J., Yaccoby, S., Sawyer, J., Burington, B., et al. (2006). The molecular classification of multiple myeloma. Blood *108*, 2020–2028.

37. Wu, G. (2009). Amino acids: metabolism, functions, and nutrition. Amino Acids *37*, 1–17.

38. Harris, D.C., Ibels, L.S., Ravich, R.B., Isbister, J.P., and Wells, J.V. (1983). Multiple myeloma with renal failure. A case for intensive treatment. Aust. N. Z. J. Med. *13*, 163–167.

39. Wu, J., Shen, J., Wang, W., Jiang, N., Jin, H., Che, X., Ni, Z., Fang, Y., and Mou, S. (2022). A novel contrast-induced acute kidney injury mouse model based on low-osmolar contrast medium. Ren. Fail. *44*, 1345–1355.

40. Zhang, J., Shi, F., Liu, X., Wu, X., Hu, C., Guo, J., Yang, Q., Xia, J., He, Y., An, G., et al. (2023). Proline promotes proliferation and drug resistance of multiple myeloma by downregulation of proline dehydrogenase. Br. J. Haematol. *201*, 704–717.

41. Kuang, C., Xia, M., An, G., Liu, C., Hu, C., Zhang, J., Liu, Z., Meng, B., Su, P., Xia, J., et al. (2023). Excessive serine from the bone marrow microenvironment impairs megakaryopoiesis and thrombopoiesis in multiple myeloma. Nat. Commun. *14*, 2093.

42. Baruch, E.N., Youngster, I., Ben-Betzalel, G., Ortenberg, R., Lahat, A., Katz, L., Adler, K., Dick-Necula, D., Raskin, S., Bloch, N., et al. (2021). Fecal microbiota transplant promotes response in immunotherapy-refractory melanoma patients. Science *371*, 602–609.

43. Nath, K.A., Hostetter, M.K., and Hostetter, T.H. (1991). Increased ammoniagenesis as a determinant of progressive renal injury. Am. J. Kidney Dis. *17*, 654–657.

44. Bosoi, C.R., and Rose, C.F. (2009). Identifying the direct effects of ammonia on the brain. Metab. Brain Dis. *24*, 95–102.

45. Jia, B., Yu, Z.J., Duan, Z.F., Lü, X.Q., Li, J.J., Liu, X.R., Sun, R., Gao, X.J., Wang, Y.F., Yan, J.Y., and Kan, Q.C. (2014). Hyperammonaemia induces hepatic injury with alteration of gene expression profiles. Liver Int. *34*, 748–758.

46. Ortiz-Pujols, S., Jones, S.W., Short, K.A., Morrell, M.R., Bermudez, C.A., Tilley, S.L., and Cairns, B.A. (2014). Management and sequelae of a 41-year-old Jehovah's Witness with severe anhydrous ammonia inhalation injury. J. Burn Care Res. *35*, e180–e183.

47. Lang, W., Blöck, T.M., and Zander, R. (1998). Solubility of NH3 and apparent pK of NH4+ in human plasma, isotonic salt solutions and water at 37 degrees C. Clin. Chim. Acta *273*, 43–58.

48. Weiner, I.D., and Verlander, J.W. (2013). Renal ammonia metabolism and transport. Compr. Physiol. *3*, 201–220.

49. Qiu, J., Tsien, C., Thapalaya, S., Narayanan, A., Weihl, C.C., Ching, J.K., Eghtesad, B., Singh, K., Fu, X., Dubyak, G., et al. (2012). Hyperammonemia-mediated autophagy in skeletal muscle contributes to sarcopenia of cirrhosis. Am. J. Physiol. Endocrinol. Metab. *303*, E983–E993.

50. Charak, B.S., Louie, R., Malloy, B., Twomey, P., and Mazumder, A. (1991). The effect of amphotericin B, aztreonam, imipenem and cephalosporins on the bone marrow progenitor cell activity. J. Antimicrob. Chemother. *27*, 95–104.

51. Davies, N.A., Wright, G., Ytrebø, L.M., Stadlbauer, V., Fuskevåg, O.M., Zwingmann, C., Davies, D.C., Habtesion, A., Hodges, S.J., and Jalan, R. (2009). L-ornithine and phenylacetate synergistically produce sustained reduction in ammonia and brain water in cirrhotic rats. Hepatology *50*, 155–164.

52. Wu, Y., Chen, H., Lu, J., Zhang, M., Zhang, R., Duan, T., Wang, X., Huang, J., and Kang, T. (2015). Acetylation-dependent function of human single-stranded DNA binding protein 1. Nucleic Acids Res. *43*, 7878–7887.

53. Collins, T.J. (2007). ImageJ for microscopy. Biotechniques *43*, 25–30.

54. Bolger, A.M., Lohse, M., and Usadel, B. (2014). Trimmomatic: a flexible trimmer for Illumina sequence data. Bioinformatics *30*, 2114–2120.

55. Langmead, B., and Salzberg, S.L. (2012). Fast gapped-read alignment with Bowtie 2. Nat. Methods *9*, 357–359.

56. Wood, D.E., and Salzberg, S.L. (2014). Kraken: ultrafast metagenomic sequence classification using exact alignments. Genome Biol. *15*, R46.

57. Patro, R., Duggal, G., Love, M.I., Irizarry, R.A., and Kingsford, C. (2017). Salmon provides fast and bias-aware quantification of transcript expression. Nat. Methods *14*, 417–419.

58. Dixon, P. (2003). VEGAN, a package of R functions for community ecology. J. Veg. Sci. *14*, 927–930.

59. Robin, X., Turck, N., Hainard, A., Tiberti, N., Lisacek, F., Sanchez, J.C., and Müller, M. (2011). pROC: an open-source package for R and S+ to analyze and compare ROC curves. BMC Bioinf. *12*, 77.

60. Soneson, C., Love, M.I., and Robinson, M.D. (2015). Differential analyses for RNA-seq: transcript-level estimates improve gene-level inferences. F1000Res. *4*, 1521.

61. Maeda, H., Fujimoto, C., Haruki, Y., Maeda, T., Kokeguchi, S., Petelin, M., Arai, H., Tanimoto, I., Nishimura, F., and Takashiba, S. (2003). Quantitative real-time PCR using TaqMan and SYBR Green for Actinobacillus actinomycetemcomitans, Porphyromonas gingivalis, Prevotella intermedia, tetQ gene and total bacteria. FEMS Immunol. Med. Microbiol. *39*, 81–86.

62. Gutiérrez-de-Juan, V., López de Davalillo, S., Fernández-Ramos, D., Barbier-Torres, L., Zubiete-Franco, I., Fernández-Tussy, P., Simon, J., Lopitz-Otsoa, F., de Las Heras, J., Iruzubieta, P., et al. (2017). A morphological method for ammonia detection in liver. PLoS One *12*, e0173914.

63. van Winden, W.A., Wittmann, C., Heinzle, E., and Heijnen, J.J. (2002). Correcting mass isotopomer distributions for naturally occurring isotopes. Biotechnol. Bioeng. *80*, 477–479.

64. Trefely, S., Ashwell, P., and Snyder, N.W. (2016). FluxFix: automatic isotopologue normalization for metabolic tracer analysis. BMC Bioinf. *17*, 485.

STAR★METHODS

KEY RESOURCES TABLE

REAGENT or RESOURCE	SOURCE	IDENTIFIER
Antibodies		
Rabbit polyclonal anti-GAPDH	Protein Tech	Cat# 10494-1-AP
Rabbit polyclonal anti-SLC12A2	Protein Tech	Cat# 13884-1-AP
Rabbit polyclonal anti-p300	Protein Tech	Cat# 20695-1-AP
Mouse monoclonal anti-β actin	Protein Tech	Cat# 66009-1-Ig
Rabbit polyclonal anti-NEK2	Protein Tech	Cat# 24171-1-AP
Mouse monoclonal anti-DYKDDDDK tag	Protein Tech	Cat# 66008-4-Ig
Mouse monoclonal anti-HA tag	ABclonal	Cat# AE008
Rabbit polyclonal anti-HDAC2	ABclonal	Cat# A2084
Rabbit monoclonal anti-HDAC3	ABclonal	Cat# A19537
Rabbit monoclonal anti-HDAC6	ABclonal	Cat#A3572
Rabbit monoclonal anti-PCAF	ABclonal	Cat# A22719
Rabbit polyclonal anti-CBP	ABclonal	Cat# A17096
Mouse monoclonal anti-NEK2 (clone D-8)	Santa Cruz	Cat# sc-55601
Rabbit monoclonal anti-Ubiquitin (clone E6K4Y)	Cell Signaling Tech	Cat# 20326
Rabbit polyclonal anti-Acetylated-Lysine	Cell Signaling Tech	Cat# 9441
Rabbit monoclonal anti-HA Tag	Cell Signaling Tech	Cat# 3724
Rabbit anti-Goat IgG Secondary Antibody HRP conjugated	Signalway Antibody	Cat# L3042
HRP-conjugated goat anti-mouse IgG secondary antibody	Signalway Antibody	Cat# 101
IPKine HRP, Mouse Anti-Rabbit IgG LCS	Abbkine Scientific	Cat# A25022
7-AAD	BD Biosciences	Cat# 559925
PI	YEASEN	Cat# 40304ES60
Alexa Fluor 647-conjugated Annexin V	YEASEN	Cat# 40304ES60
CD138 MicroBeads human	Miltenyi Biotec	Cat# 130-051-301
Bacterial and virus strains		
pLKO-Tet-on lentiviral vector	Xiangling Feng et al.[8]	N/A
pMD2G helper vectors	Xiangling Feng et al.[8]	N/A
psPAX2 helper vectors	Xiangling Feng et al.[8]	N/A
Citrobacter freundii	Beijing BeiNa Biotechnology Institute	BNCC 186116
Clostridium butyricum	Beijing BeiNa Biotechnology Institute	BNCC 337239
Klebsiella oxytoca	Beijing BeiNa Biotechnology Institute	BNCC358247
Raoultella ornithinolytica	Beijing BeiNa Biotechnology Institute	BNCC341928
BIO THREE TABLETS (Triple probiotic tablet)	Huizhou Jiuhui Pharmaceutical	N/A
Biological samples		
Feces of patients with MM	Xiangya Hospital, the Third Xiangya Hospital of Central South University, and the Blood Diseases Hospital of the Chinese Academy of Medical Science & Peking Union Medical College	N/A

(*Continued on next page*)

Continued

REAGENT or RESOURCE	SOURCE	IDENTIFIER
Serum samples	Xiangya Hospital, the Third Xiangya Hospital of Central South University, and the Blood Diseases Hospital of the Chinese Academy of Medical Science & Peking Union Medical College	N/A
Chemicals, peptides, and recombinant proteins		
Furosemide sodium	Selleck Chemicals	S5194; CAS: 41733-55-5
NH_4Cl	Sigma-Aldrich	A9434; CAS: 12125-02-9
$^{15}NH_4Cl$	Sigma-Aldrich	917281; CAS: 39466-62-1
Glycine	Sigma-Aldrich	G8790; CAS: 56-40-6
Polybrene	Sigma-Aldrich	Cat# H9268
Cycloheximide	MedChemExpress	HY-12320; CAS: 66-81-9
MG132	MedChemExpress	HY-13259; CAS: 133407-82-6
Bortezomib	Janssen	N/A
Low melting point agarose	Thermo Fisher Scientific	Cat# 16520050
Lipofectamine 3000	Thermo Fisher Scientific	Cat# L3000015
SuperSignal West Femto Maximum Sensitivity Substrate	Thermo Fisher Scientific	Cat# 34094
Lithium dodecyl sulfate	Thermo Fisher Scientific	Cat# B0007
Puromycin	Thermo Fisher Scientific	Cat# A1113803
Ampicillin	Solarbio	Cat# A8180; CAS: 69-52-3
Vancomycin	Solarbio	Cat# V8050; CAS: 1404-93-9
Neomycin	Solarbio	Cat# N8090; CAS: 1405-10-3
Metronidazole	Solarbio	Cat# M8060; CAS: 443-48-1
Kanamycin	Solarbio	Cat# K8020; CAS: 25389-94-0
Protein A/G beads	Biolinkedin	Cat# L-1004A
Critical commercial assays		
Apoptosis Detection Kit	YEASEN	Cat# 40304ES60
VivoGlo Luciferin	Promega	Cat# P1043
ChamQ Universal SYBR qPCR Master Mix	Vazyme	Cat# Q711-02
Mouse IgG2b ELISA Quantitation Set	BETHYL	Cat# E90-109
Acetyl CoA Assay	Cell Signaling Tech	Cat# ab87546
Nessler's reagent	Sigma-Aldrich	Cat# 109028
Blood Ammonia Assay Kit	Nanjing Jiancheng Biotechnology	Cat# A086
Deposited data		
$CD138^+$ selected plasma cells from bone marrow of patients with multiple myeloma	Gene Expression Omnibus (GEO) database (GSE2658)	https://www.ncbi.nlm.nih.gov/geo/query/acc.cgi?acc=GSE2658
ARP1 RNA-Seq	This paper	http://bigd.big.ac.cn/gsa-human/s/3kUd5023
Metagenomic sequencing	This paper	http://bigd.big.ac.cn/gsa-human/s/3kUd5023
Experimental models: Cell lines		
ARP1	Cancer Research Institute of the Central South University	N/A
H929	Cancer Research Institute of the Central South University	N/A
5TGM1	Cancer Research Institute of the Central South University	N/A
Experimental models: Organisms/strains		
Mouse: Wildtype: C57BL/6J	The Jackson Laboratory	N/A

(*Continued on next page*)

Continued		
REAGENT or RESOURCE	SOURCE	IDENTIFIER
Mouse: C57BL/KaLwRij	Harlan Mice, Netherlands	N/A
Mouse: NOD/ShiLtJGpt-Prkdc^{em26Cd52}Il2rg^{em26Cd22}/Gpt	GemPharmatech	Cat# T001475
Mouse: NOD.CB17-Prkdc^{scid}Il2rg^{tm1}/Bcgen	Biocytogen	N/A
Oligonucleotides		
List of primers	Table S7	N/A
Recombinant DNA		
pKO3-km	Xingxing Jian et al.[18]	N/A
pBbE8k-RFP	addgene	Cat# 35270
PCDH-GFP	Xiangling Feng et al.[8]	N/A
pCDNA3.1 vector	Yuanzhong Wu et al.[52]	N/A
Software and algorithms		
ImageJ	Tony J Collins[53]	https://imagej.nih.gov/ij/
Living Imaging version 3.2	PerkinElmer	https://www.perkinelmer.com.cn/lab-products-and-services/resources/in-vivo-imaging-software-downloads.html
Graphpad prism version 9.5	GraphPad	https://www.graphpad.com/
FlowJo version 10.6.2.	BD Biosciences	https://www.flowjo.com/solutions/flowjo/downloads
SageCapture software version 2.17.12.170316	Sagecreation	N/A
Trimmomatic version 0.36	Anthony M Bolger et al.[54]	https://kbase.us/applist/apps/kb_trimmomatic/run_trimmomatic/release
Bowtie2 version 2.2.4	Ben Langmead et al.[55]	https://sourceforge.net/projects/bowtie-bio/files/bowtie2/2.2.4/
Kraken version 1.0	Derrick E Wood et al.[56]	https://github.com/DerrickWood/kraken
Salmon version 1.10.1	Rob Patro et al.[57]	https://salmon.readthedocs.io/en/latest/salmon.html
R version 4.1.2	CRAN	https://cran.r-project.org/bin/windows/base/old/
R package vegan version 2.5–2	Dixon Philip[58]	https://cran.r-project.org/src/contrib/Archive/vegan/
R package DESeq2 version 1.38.0	Bioconductor	https://bioconductor.org/packages/release/bioc/html/DESeq2.html
R package randomForest version 4.7–1.1	Machine Learning	https://cran.r-project.org/src/contrib/Archive/randomForest/
R package pROC version 1.18.0	Xavier Robin et al.[59]	https://cran.r-project.org/src/contrib/Archive/pROC/
R package tximport version 1.20.0	Charlotte Soneson et al.[60]	http://bioconductor.org/packages/release/bioc/html/tximport.html

RESOURCE AVAILABILITY

Lead contact

Further information and requests for resources and reagents should be directed to and will be fulfilled by the lead contact is Dr. Zhou, who can be reached at wenzhou@csu.edu.cn.

Materials availability

All unique and stable reagents including cell lines that were generated in the course of this study are available from the lead contact with a completed Materials Transfer Agreement.

Data and code availability

- All sequencing reads have been deposited in the Genome Sequence Archive in National Genomics Data Center, China National Center for Bioinformation/Beijing Institute of Genomics, Chinese Academy of Sciences (http://bigd.big.ac.cn/gsa-human/s/3kUd5023), in which the accession number of metagenomic sequencing samples and ARP1 cells cultured with and without NH_4^+ are GSA: HRA005114 and GSA: HRA005226, respectively. Transcriptome datasets (GEO: GSE2658) involved in $CD138^+$ cells sorted from the BM of patients with MM or healthy donors was downloaded from public GEO database (https://www.ncbi.nlm.nih.gov/geo/). Data generated in this study is available in the supplementary tables. Any raw data requested that was generated in this study is available in the Data S1.
- This paper does not report any original code.
- Any additional information required to reanalyze the data reported in this paper is available from the lead contact upon request.

EXPERIMENTAL MODEL AND SUBJECT DETAILS

Mice

All mice used in this paper are in a predominant C57BL/6 or NOD background. Males and females are equally represented, and littermates were randomly mixed in all experimental conditions. The mice were housed in a temperature controlled, specific pathogen free environment, with a 12 h light/dark cycle. They were fed *ad libitum* with standard chow diet. Studied mice were between 8 and 12 weeks old. B-NDG mice from Biocytogen and NCG mice from GemPharmatech were used for the xenograft tumor studies. All animal experiments were performed in accordance with the guidelines of the Institutional Animal Care and Local Veterinary Office and Ethics Committee of the Hunan Normal University, China (License number: D2022058).

Patients and clinical samples

This study is a retrospective study. All samples shown in Table S5 were obtained from the Xiangya Hospital, the Third Xiangya Hospital of Central South University, and the Blood Diseases Hospital of the Chinese Academy of Medical Science & Peking Union Medical College, including 20 healthy controls (HC), 159 patients with MM at diagnosis (AD), 67 relapsed patients with MM (RM). In total, we collected 190 fecal samples and 73 serum samples. The fecal samples were used for metagenomic sequencing, qPCR verification, and NH_4^+ detection, while serum samples were used for NH_4^+ detection (Table S5). The Xiangya Hospital of the Central South University (CSU) Medical Ethics Committee approved the study protocols (License number: 2019030391), and written informed consent was obtained before the investigation. All the research was carried out in accordance with the provisions of the Helsinki Declaration of 1975.

Human survival analysis

Human survival analysis was determined using the Graphpad prism version 9.5. Significance is computed using the Cox-Mantel log-rank test.

Cell lines

Human multiple myeloma cell lines ARP1, ARP1-BR, H929, and H929-BR were used for most experiments. Mouse multiple myeloma cell line 5TGM1 used in animal experiments. Cell lines have been STR-authenticated. All cells were maintained in complete Roswell Park Memorial Institute (RPMI) 1640 medium (supplemented with 10% fetal bovine serum and 1% antibiotic/antimycotic agent) at 37 °C in 5% CO_2 and 21% O_2.

METHOD DETAILS

Metagenomic sequencing and taxonomic classification

Total DNA was extracted from fecal samples using the E.Z.N.A Stool DNA Kit (Omega Bio-tek, Norcross, GA, USA) following the manufacturer's instructions. Quality analysis was performed using Qubit (Invitrogen, USA) and 1% agarose gel electrophoresis, and the extracted DNA was then used for paired-end sequencing on the Illumina platform.

Quality control as conducted on the raw sequences to remove low-quality and adapter sequences by using Trimmomatic version 0.36, and Bowtie2 version 2.2.4 was used to filter out the human reference genome (hg38). The high-quality sequences were then used for taxonomic classification using Kraken version 1.0 and the standard Kraken database with default settings. The output read-count tables at several levels (e.g., phylum, class, order, family, genus, species) were rarefied to the minimum read counts to reduce the effects of uneven sampling by R package vegan version 2.5–2.

Real-time quantitative PCR (qPCR)

Three differential species identified by metagenomic sequencing were verified by qPCR. Total bacterial DNA was extracted using the HiPure Stool DNA Kit (#D3141-03, Magen, China) according to the manufacturer's instructions. Paired primers specific for each species were designed using Primerblast based on species-specific regions of the 16S ribosomal DNA (V1 or V2), while the conserved sequences were used for amplification of total bacteria (Table S7).[61] All primers were validated using gradient PCR to detect the

annealing temperature and the specificity of primers. qPCR assays were performed by using ChamQ Universal SYBR qPCR Master Mix (#Q711-02, Vazyme, China) according to the manufacturer's instructions. qPCR was run on a LightCycler 96 system (Roche).

As in a previous study,[18] assuming that for all templates and primers a cycle equally doubles the number of template DNA strands, the relative abundance of a certain strain (i) can be calculated as follows:

$$\text{Relative abundance (i)} = \frac{\left(\frac{1}{2}\right)^{CTi}}{\left(\frac{1}{2}\right)^{CTc}} = \left(\frac{1}{2}\right)^{CTi-CTc} = \left(\frac{1}{2}\right)^{\Delta CT}$$

The cycle threshold of strain i primer and common primer (total bacteria) are represented by CTi and CTc, while △CT denotes the difference between them. From the equation, the logarithm of relative abundance negatively correlates linearly with △CT.

Bacterial diversity

Rarefaction analysis was performed by using R package vegan version 2.5–2. This package was also used to evaluate the Bray-Curtis dissimilarity indices to reflect beta-diversity, and these indices were then visualized by performing principal coordinate analysis (PCoA). The permutational multivariate analysis of variance (PERMANOVA) was used to determine significance. The Shannon indexes at both species and genus level were estimated by R package vegan to reflect bacterial α-diversity, and the significance was determined by Wilcoxon rank-sum test.

Mouse xenograft models of MM

All animal experiments were performed in accordance with the guidelines of the Institutional Animal Care and Local Veterinary Office and Ethics Committee of the Hunan Normal University, China (License number: D2022058). Here, C57BL/KaLwRij mice (Harlan Mice, Netherlands), B-NDG mice (NOD.CB17-Prkdcscidll2rgtm1/Bcgen, Biocytogen, Beijing, China) and NCG mice (NOD/ShiLtJGpt-Prkdc^{em26Cd52}Il2rg^{em26Cd22}/Gpt, GemPharmatech, Jiangsu, China) were used in this study. The 5TGM1 MM model was developed by intravenously injecting luciferase-expressing 5TGM1 cells (1×10^6 cells in 200 μL PBS) into C57BL/KaLwRij mice. MM progression in the mice was monitored by measuring the tumor burden, including live imaging and serum IgG2b measurement. ELISA was performed for the detection of mouse IgG2b in serum using Mouse IgG2b ELISA Quantification Set (#E90-109, Bethyl Laboratories, USA). The ARP1 MM mouse xenograft model was developed by intravenously injecting luciferase-expressing ARP1 cells (1×10^6 cells in 200 μL PBS) into B-NDG/NCG mice, and MM progression in the mice was monitored by measuring the tumor burden via live imaging.

Fecal microbiota transplantation

Fresh stool (0.5 g) was collected and suspended in PBS (10 mL). The suspension was filtered using 70 μm strainers, and the filtrate was centrifuged at 2,000 rpm for 10 min. After removal of the supernatant, the remaining pellet was re-suspended in 2 mL PBS. The mixture was used for subsequent fecal microbiota transplantation (FMT) by gavage (200 μL/mouse). Table S5 provides detailed patient information.

Before gavage was performed, all experimental mice were treated with a cocktail of broad-spectrum antibiotics including ampicillin (200 mg/mL), vancomycin (100 mg/mL), neomycin (200 mg/mL), and metronidazole (200 mg/mL) in the drinking water for 2 weeks. Subsequently, all mice were randomly divided into several groups to receive 2 weeks FMT (once per 2 days in the first week and once per 3 days in the second week). Meanwhile, the control mice were given PBS by gavage. Then, at week 0, C57BL/KaLwRij mice were induced to develop MM via tail-vein injection of 5TGM1 cells (1×10^6). From week 1, if required, BTZ (0.75 mg/kg every 2 days) and furosemide sodium (10 mg/kg every day) were intraperitoneally administered. At the endpoint of the experiment, tumor burden was assessed in all experimental mice using live imaging of tumors, serum IgG2b, fecal samples, and cecal content for subsequent detection.

Bacterial fluid colonization

We purchased *Citrobacter freundii* (BNCC 186116), *Klebsiella oxytoca* (BNCC358247), *Raoultella ornithinolytica* (BNCC341928) and *Clostridium butyricum* (BNCC 337239) from Beijing BeiNa Biotechnology Institute. *Citrobacter freundii* was cultured in nutrient broth (Guangdong HuanKai Microbial, China) at 37 °C and 200 rpm for ~16 h, while *Clostridium butyricum* was statically cultured in thioglycolate medium (Qingdao Hope Bio Technology Co., Ltd., China) under anaerobic conditions at 37 °C for ~18 h. The bacterial concentration was about 2×10^8 cfu/200 μL. In addition, we dissolved four 200mg triple-probiotic tablets (Huizhou Jiuhui Pharmaceutical Co., LTD, Guangzhou, China) containing *Clostridium butyricum*, *Bacillus mesentericus* and, *Streptococcus faecalis* and dissolved them in sterile water (3 mL) for subsequent colonization (200 μL/mice).

In the colonization experiment involving *Citrobacter freundii*, *Klebsiella oxytoca* and *Raoultella ornithinolytica*, before C57BL/KaLwRij mice were treated with a cocktail of broad-spectrum antibiotics in the drinking water for 2 weeks, then, mice were transplanted bacterial fluid by gavage (200 μL/mouse; once per 3 days) for 1 week prior to induction of MM via tail-vein injection of 5TGM1 cells at week 0. As our bacterial cells were resuspended in PBS, the control mice were given PBS by gavage. After 1 week, mice were transplanted bacterial fluid by gavage (200 μL/mouse; once per 3 days), or injected intraperitoneally with BTZ

(0.75 mg/kg; once per 2 days). At the endpoint of the experiment, all mice were assessed via live imaging and the collection of serum samples, fecal samples, and cecal content for subsequent detection.

In the colonization experiment involving wild-type and disrupted *Citrobacter freundii*, before C57BL/KaLwRij mice were treated with a cocktail of broad-spectrum antibiotics in the drinking water for 2 weeks, then, mice were transplanted bacterial fluid by gavage (200 μL/mouse; once per 3 days) for 1 week prior to induction of MM via tail-vein injection of 5TGM1 cells at week 0. As our bacterial cells were resuspended in PBS, the control mice were given PBS by gavage. After 1 week, mice were transplanted bacterial fluid by gavage (200 μL/mouse; once per 3 days), or injected intraperitoneally with BTZ (0.75 mg/kg; once per 2 days), or treated intragastrically with NH_4^+ (5.35 mg/mL, 150 μL/mouse). At the endpoint of the experiment, all mice were assessed via live imaging and the collection of serum samples, fecal samples, and cecal content for subsequent detection.

In the colonization experiment of *Clostridium butyricum* and triple probiotics, before C57BL/KaLwRij mice were treated with a cocktail of broad-spectrum antibiotics in the drinking water for 2 weeks prior to induction of MM via tail-vein injection of 5TGM1 cells at week 0. Subsequently, mice were transplanted with Kanamycin-resistant *Citrobacter freundii* or PBS by gavage for 2 weeks (200 μL/mice; once per 3 days), and mice were treated with kana (400 mg/mL) in the drinking water for 1 week. Mice were then respectively transplanted with bacterial fluid (i.e.,.*Clostridium butyricum* or triple probiotics) by gavage (once per 3 days), or injected intraperitoneally with BTZ (0.75 mg/kg; once per 2 days). At the endpoint of experiment, all mice were applied for measuring the tumor burden, including live imaging and serum IgG2b concentration, collected serum samples, fecal samples, and cecal content for subsequent detection. At the endpoint of the experiment, tumor burden was assessed in all experimental mice using live imaging of tumors, serum IgG2b concentrations, fecal samples, and cecal content for subsequent detection.

Ammonium transplantation experiment and sample collection

In the ammonium transplantation experiment, C57BL/KaLwRij or B-NDG mice were treated intragastrically with NH_4^+ (5.35 mg/mL, 150 μL/mouse) for 1 week (once per day) prior to induction of MM via tail-vein injection of 5TGM1 or ARP1 cells.

Then, starting from week 1, BTZ (0.75 mg/kg) was injected intraperitoneally into the abdomen of mice (once per 2 days), with 0.9% NaCl used to treat controls. At the endpoint of the experiment, all mice were assessed via live imaging and the collection of serum samples, fecal samples, and cecal content for subsequent detection. The concentration of NH_4^+ was detected using the Blood Ammonia Assay Kit (#A086, Nanjing Jiancheng Biotechnology, China).

Experiment of furosemide sodium-assisted BTZ in the treatment of MM

In the experiment of furosemide sodium treatment, before induction of MM via tail-vein injection of 5TGM1 cells, mice were given NH_4^+ (5.35 mg/mL, 150 μL/mouse) intragastrically (once per day) for 1 week in advance until the end of the experiment. Simultaneously, starting from week 1, mice were injected intraperitoneally with BTZ (0.75 mg/kg; once per 2 days) or furosemide sodium (10 mg/kg; once per day) into the abdomen. At the endpoint of experiment, the experimental mice were applied for tumor burden detection, and collected serum samples, fecal samples, and cecal content for subsequent detection.

ARP1-NEK2sh experiment and sample collection

In the ARP1-NEK2sh experiment, B-NDG mice were treated intragastrically with NH_4^+ (5.35 mg/mL, 150 μL/mouse) for 1 week (once per day) prior to induction of MM via tail-vein injection of ARP1-Scr/ARP1-NEK2sh cells.

Then, starting from week 0, NH_4^+ (5.35 mg/mL, 150 μL/mouse) was treated intragastrically into the abdomen of mice (once per day), with 0.9% NaCl used to treat controls. At the endpoint of the experiment, all mice were assessed via live imaging and the collection of serum samples, cecal content and $CD138^+$ cells for subsequent detection. The concentration of NH_4^+ was detected using the Blood Ammonia Assay Kit (#A086, Nanjing Jiancheng Biotechnology, China).

ARP1-SLC12A2sh experiment and sample collection

In the ARP1-SLC12A2sh experiment, NCG mice were treated intragastrically with NH_4^+ (5.35 mg/mL, 150 μL/mouse) for 1 week (once per day) prior to induction of MM via tail-vein injection of ARP1-Scr/ARP1-SLC12A2sh cells.

Then, starting from week 1, BTZ (0.75 mg/kg) was injected intraperitoneally into the abdomen of mice (once per 2 days), with 0.9% NaCl used to treat controls. At the endpoint of the experiment, all mice were assessed via live imaging and the collection of serum samples, cecal content and $CD138^+$ cells for subsequent detection. The concentration of NH_4^+ was detected using the Blood Ammonia Assay Kit (#A086, Nanjing Jiancheng Biotechnology, China).

Experiment of furosemide sodium-assisted BTZ in the treatment of MM-BR

In the experiment of furosemide sodium treatment, induction of MM via tail-vein injection of ARP1/ARP1-BR cells. Simultaneously, starting from week 1, mice were injected intraperitoneally with BTZ (0.75 mg/kg; once per 2 days) or furosemide sodium (5 mg/kg; once per day) into the abdomen. At the endpoint of experiment, the experimental mice were applied for tumor burden detection, and collected serum samples, cecal content and $CD138^+$ cells for subsequent detection.

Construction of deaminase-deletion *Citrobacter freundii*

The NCBI database lists nine genes that encode deaminases in *Citrobacter freundii*, including cytosine deaminase (cyd, NZ_CP033744.1), cytidine deaminase (cdd, NZ_CP033744.1), adenosine deaminase (add, NZ_CP033744.1), dCTP deaminase

(dad, NZ_CP033744.1), tRNA adenosine deaminase (tadA, NZ_CP033744.1), 2-iminobutanoate/2-iminopropanoate deaminase (ridA, NZ_CP033744.1), enamine/imine deaminase (end, NZ_CP033744.1), glucosamine-6-phosphate deaminase (nagB, NZ_CP033744.1), and bifunctional diaminohydroxyphosphoribosylaminopyrimidine deaminase/5-amino-6-(5-phosphoribosylamino) uracil reductase (ribD, NZ_CP033744.1). The primers used in this study to examine the expression of these nine genes by qPCR are listed in Table S7.

The *end*-deletion and *add*-deletion *Citrobacter freundii* were constructed by homologous recombination using the plasmid pKO3-km as we previously reported.[18] We selected strains end-5 and add-1 to examine NH_4^+ production, and the end-deletion *Citrobacter freundii* was used for subsequent mice experiments, as described in bacterial fluid colonization. There was no significant difference in the growth of wild type vs. disrupted *Citrobacter freundii* according to the turbidity/absorbance of the fermentation broth.

Nessler's staining of biological tissues

Nessler's reagent staining was performed as described.[62] Briefly, tissues were embedded in paraffin and sectioned into 5 μm. The slides were then subjected to dewaxing and rehydration treatment. Slides were washed for 5 min with sterile distilled water, and incubated 5 min with Nessler's reagent, then washed for 10 s, then counterstained with hematoxylin, washed with running water for 60 s, then dehydrated briefly and mounted on slides for imaging. Nessler's reagent is composed of 2 g potassium iodide, 3 g mercury iodide and 40 g potassium hydroxide in 20 mL of water.

Immunocytochemistry

The collected small intestine and tibia samples from the experimental mice were fixed with paraformaldehyde, embedded in paraffin after dehydration and sliced for immunohistochemistry. The slides were then subjected to dewaxing, rehydration and hydrogen peroxide treatment before incubating with anti-SLC12A2 antibody at a 1:2000 dilution overnight at 4 °C. Next, the slides were incubated with HRP-conjugated secondary antibody and stained with 3,3′-diaminobenzidine tetrahydrochloride hydrate (DAB) for 3 min. Finally, cell nuclei were counterstained with hematoxylin.

Western blotting

Proteins were extracted using radio immunoprecipitation assay (RIPA) lysis buffer (#P0013B, Beyotime, China) and quantified with a BCA Protein Quantification Kit (#E112-01, Vazyme, China). Proteins were separated by sodium dodecyl sulfate polyacrylamide gel electrophoresis (SDS-PAGE) and transferred to a 0.45 μm polyvinylidene fluoride membrane (#ISEQ00010, Millipore, USA). The membrane was blocked using 5% BSA in Tris-buffered saline solution containing 0.1% Tween 20 (TBS-T) for 1 h at room temperature and then probed with specific primary antibodies overnight at 4 °C. Subsequently, the membranes were washed with TBS-T followed by incubation with HRP-conjugated secondary antibodies for 1 h at room temperature. GAPDH was used as the protein loading control. Protein signals were developed with SuperSignal West Femto Maximum Sensitivity Substrate (#34094, Thermo Fisher Scientific, USA) and imaged using a MiniChemi 610 chemiluminescence imaging system with SageCapture software version 2.17.12.170316 (Sagecreation, China).

Acetyl CoA assay

Harvest ~1×10^7 cells, and suspend the cell pellet in 1000 μL of the assay buffer on ice. Homogenize using a Dounce homogenizer on ice for 10–50 passes until efficient lysis is confirmed by viewing the cells under a microscope. Spin homogenate at 10,000 × g for 10 min at 4 °C. Collect the supernatant on ice. Perform deproteinization in ice-cold perchloric acid (PCA) 4M to a final concentration of 1 M in the homogenate solution and vortex briefly to mix well. After 5 min, add ice-cold 2 M KOH, after neutralization, centrifuge samples at 13,000 × g for 15 min at 4 °C in a cold centrifuge and transfer supernatant to a fresh tube. The samples are now ready to use in the assay.

Soft agar clonogenicity assay

We mixed 3.5% low melting point agarose (#16520050, Thermo Fisher Scientific) and media in a 1:4 ratio to prepare the bottom soft agar and then quickly added it into 12-well plates (1 mL soft agar/well). After the bottom soft agar solidified, the upper soft agar was prepared through mixing 1.66% low melting point agarose and media containing MM cells at a 1:4 ratio. Upper soft agar was added onto the surface of bottom soft agar (0.5 mL soft agar/well), and the cell densities were as follows: ARP1, 1,000 cells/well in normal media; H929, 2,000 cells/well in normal media. Cells were fed with media supplemented with or without drugs twice every week. One colony was defined if more than 50 cells were observed. Plates were imaged under inverted microscope, and colonies were enumerated using ImageJ software. Each sample was repeated three times.

Vectors, transfections, and transductions

Short hairpin RNA (shRNA) sequences targeting human SLC12A2 were obtained from the RNAi Consortium collection (MISSION shRNA; Sigma-Aldrich). shRNA sequences were annealed and ligated into a pLKO-Tet-on lentiviral vector. Lentiviruses were packaged in HEK293T cells using pMD2G and psPAX2 helper vectors and polybrene (3 μg/mL)-mediated transduction (#H9268-5G, Sigma-Aldrich). Transient transfection was performed using Lipofectamine 3000 reagent (#L3000015, Thermo Fisher Scientific) according to the manufacturer's instructions. MM cells transduced with recombinant lentivirus were selected with 1–2 μg/mL puromycin (#A1113803, Thermo Fisher Scientific). shRNA sequences were obtained from Tsingke Biotechnology. All shRNA sequences are listed in Table S7.

NEK2 point mutation fragments were ligated into a PCDH-GFP lentiviral vector. Lentiviruses were packaged as mentioned earlier. pCDNA3.1-HA-PCAF, pCDNA3.1-HA-p300, pCDNA3.1-HA-CBP, pCDNA3.1-HA-GCN5, pCDNA3.1-HA-Tip60, pCDNA3.1-FLAG-HDAC1, pCDNA3.1-FLAG-HDAC2, pCDNA3.1-FLAG-HDAC3, pCDNA3.1-FLAG-HDAC6 and pCDNA3.1-FLAG-HDAC10 were gifts from Prof. Tiebang Kang (Sun Yat-sen University).

Ammonia tracing

As described in a previous publication,[63] we washed ARP1 cells were twice with PBS. Then, cells (1×10^7) were seeded in a 10 cm dish in RPMI 1640 media (Gibco, USA) supplemented with 10% fetal bovine serum (FBS; Biological Industries, Israel) and 0.5 mM ^{15}N-NH_4Cl (Sigma-Aldrich). Cells were collected at 3, 6, and 12 h. Cell pellets were washed three times with cold PBS, and the dry pellets were stored at −80 °C for subsequent analysis.

After correcting for the natural isotope, samples were analyzed using ultra-performance liquid chromatography triple-quadrupole mass spectrometry (UPLC-TQ-MS) (Waters Corp, UK) following our previously published procedure.[64] Metabolites were separated through a 2.1 × 100 mm 1.7 μm Acquity amide and an Acquity HSS C18 column (Waters Corp) equipped with an ACQUITY UPLC VanGuard Pre-Column (Waters Corp). A 5 μL aliquot of the sample was injected into the column, which was maintained at 40 °C. The flow rate remained constant at 0.4 mL/min. The raw UPLC-MS data were analyzed using TargetLynx Application Manager software version 4.1 (Waters Corp). Quantification of each metabolite was performed by using linear regression analysis of the peak area of metabolite versus concentration.

The measurements of mass distribution vector (MDV) of ^{15}N-labeled metabolites, which describes the fractional abundance of each isotopologue normalized to the sum of all possible isotopologues, were performed in all detected metabolites. Before calculation of the MDVs of metabolites, the correction of naturally occurring isotopes was also performed based on the previous publication.[64]

RNAseq and quantitative analysis

ARP1 cells were *in vitro* cultured with and without NH_4^+ for 12h, and then we harvested 1×10^6 cells for paired-end RNAseq on the Illumina platform. Trimmomatic (version 0.36) was used to remove low-quality reads and adapter sequences. Then, the obtained high-quality reads were aligned and quantified analysis by using Salmon (version 1.10.1) and R package tximport (version 1.20.0).

Flow cytometry

Apoptotic cells were labeled with Alexa Fluor 647-conjugated Annexin V (#40304ES60, YEASEN, China). Dead cells were labeled by PI/7AAD (YEASEN). Cell staining was performed according to the manufacturer's protocol. Labeled cells were then measured by CytoFLEX (Beckman Instruments, CA, USA). The percentages of apoptotic cells were calculated using FlowJo software version 10.6.2.

Immunoprecipitation

The HEK293T, ARP1 and H929 cell lines were used for NEK2 ubiquitylation/acetylation analysis. All procedures followed the standard protocol previously reported. Briefly, cells were lysed in lysis buffer for 40 min on ice and quantified by using a BCA Protein Quantification Kit. The lysates were incubated overnight at 4 °C on a rotator with 4 μg of mouse polyclonal anti-NEK2 (Santa Cruz Biotechnology, CA, USA) or rabbit monoclonal anti-acetylation (Cell Signaling Technology, USA). 50 μL of protein A/G beads (#L-1004A, Biolinkedin, Shanghai, China) were transferred to the protein-antibody complexes, and immunoprecipitates were collected after 2 h incubation. Finally, the immunoprecipitates were re-suspended in lithium dodecyl sulfate (LDS, #B0007, Thermo Fisher Scientific, USA) sample buffer and heated for 5 min at 100 °C for analysis by LDS polyacrylamide gel-electrophoresis, loading equal concentrations of protein from the original lysate, and western blotting with monoclonal antibodies against ubiquitylation, FLAG tag and acetylation (Cell Signaling Technology, USA).

QUANTIFICATION AND STATISTICAL ANALYSIS

Metagenomic bacteria were analyzed statistically on the R platform. Here, core microbes (i.e., genus, species) were defined as gut microbes that exhibited a read-count percentage (relative abundance) greater than 0.01% and were detected in at least 90% of subjects in group. Based on the read-count matrix of those core microbes, we performed differential analysis by using R package DESeq2 version 1.26.0, and significant differences were defined based on an absolute value >1 for the log2 fold change and an adjusted p value <0.05.

In addition, those differential species were respectively applied to build classification model by R package randomForest version 4.7–1.1, in which 80% of those samples were used as the training set and 20% as the test set. The receiver operating characteristic curves (ROC) were visualized by R package pROC version 1.18.0.

All experimental data were statistically analyzed and visualized via Graphpad Prism version 9, and the significance between two groups was determined by two-tailed *t*-test.